Molecular Cancer

RESEARCH

Open Access

Targeting BATF2-RGS2 axis reduces T-cell exhaustion and restores anti-tumor immunity

Xuyu Gu[1], Chanchan Gao[2], Xiangyu Su[2], Yaoyao Zhu[3], Qiyu Fang[1], Jia Yu[1], Ziming Wang[4], Deping Zhao[4*] and Wentian Zhang[4*]

Abstract

Objective This study aims to investigate the role of RGS2 in immune regulation in lung cancer (LC) and explore the regulatory relationship between RGS2 and BATF2 in modulating T cell exhaustion and tumor immune evasion.

Methods Single-cell transcriptome-based analysis was performed to identify $CD8^+$ T-cell profiles and regulatory factors in six LC patients receiving neoadjuvant PD-1 blockade therapy. Mouse 3LL cells or murine tumor organoid models were transplanted into wild-type, RGS2 knock-out ($RGS2^{-/-}$), or BATF2 knock-out ($BATF2^{-/-}$) mice to analyze the effects of RGS2 and BATF2 on tumor growth, metastasis, and immune cell infiltration. $CD8^+$ from these mice were isolated and co-cultured with cancer cells to analyze T cell cytotoxicity in vitro. The transcriptional regulation of RGS2 by BATF2 was analyzed using luciferase reporter assays.

Results RGS2 was highly expressed in $CD8^+$ T-exhausted (Tex) cells and was associated with pro-inflammatory pathways. High RGS2 expression predicted poor clinical outcomes and limited response to PD-1/PD-L1 blockade therapy. In $RGS2^{-/-}$ mice, tumor metastasis and angiogenesis were suppressed, $CD8^+$ effector T cells were enhanced, and T cell exhaustion markers were reduced. BATF2 was identified as a key transcriptional regulator of RGS2, promoting T cell exhaustion through inhibition of CXCL13 secretion. Knockdown of BATF2 or RGS2 impaired lung cancer cell proliferation and enhanced sensitivity to NK cell-mediated cytotoxicity in vitro. In $BATF2^{-/-}$ mice, the populations of immune active $CD8^+$ T cells were increased, while exhausted T cells were reduced, leading to improved anti-tumor immune responses.

Conclusions RGS2, regulated by BATF2, plays a critical role in driving T cell exhaustion and tumor immune evasion in LC. Targeting the BATF2-RGS2 axis may enhance the effectiveness of immunotherapy by reversing T cell exhaustion and improving anti-tumor immunity.

Keywords RGS2, BATF, T-cell exhaustion, CXCL13, Immunosuppression, Lung cancer

*Correspondence:
Deping Zhao
zdp1992@163.com
Wentian Zhang
dr_zhangwentian@163.com
[1] Department of Oncology, School of Medicine, Shanghai Pulmonary Hospital, Tongji University, Shanghai 200433, China
[2] Department of Oncology, School of Medicine, Zhongda Hospital, Southeast University, Nanjing 210009, China
[3] Department of Radiation Oncology, School of Medicine, Shanghai Pulmonary Hospital, Tongji University, Shanghai 200433, China
[4] Department of Thoracic Surgery, School of Medicine, Shanghai Pulmonary Hospital, Tongji University, Shanghai 200433, China

Introduction

Lung cancer (LC) accounts for approximately 2 million new cases and 1.76 million deaths annually, making it one of the leading causes of cancer-related mortality worldwide [1]. LC is histologically classified into non-small cell lung cancer (NSCLC) and small cell lung cancer, representing approximately 85% and 15% of LC cases, respectively [2]. Key risk factors for the development of LC include tobacco, exposure to environmental pollution, occupational exposure, genetic predisposition, and chronic lung infections [3]. The fact that 75% of LC cases

are detected in advanced stages contributes to a poor prognosis, with a 5-year survival rate ranging from 4% to 17% [4].

Immunotherapy has significantly transformed cancer treatment strategies by harnessing the power of immunological memory to generate lasting therapeutic responses. It offers a generally tolerable safety profile and proves effective across a wide range of patients [5]. Cancer immunotherapy has experienced significant progress thanks to immune checkpoint inhibitors (ICIs), which include the blocking of programmed death-1 (PD-1), its ligand programmed death-ligand 1 (PD-L1), and cytotoxic T-lymphocyte-associated antigen-4 (CTLA4) [6]. Clinically, antibodies targeting PD-1/PD-L1 have been shown to rejuvenate exhausted T cells (Tex) within the tumor microenvironment (TME), leading to durable remission and impressive objective responses [7]. The presence of functional, non-exhausted T-cells within the TME is regarded as an imperative for ICIs efficacy, while T-cell exhaustion represents a major resistance pathway to immunotherapy [8]. Therefore, it is critical to explore the complex mechanisms underlying T-cell exhaustion in LC.

Regulator of G protein signaling 2 (RGS2) is a key mediator of signaling through G protein-coupled receptors (GPCRs) and is known for its selective modulation of the Gα subunit [9]. RGS2 can modulate adenylate cyclase activity and protein synthesis by protein-protein interactions, which has attracted much attention due to its role as a potential target for therapeutic drugs with clinical implications [10]. Interestingly, elevated RGS2 expression has been associated with decreased overall and disease-free survival in patients with NSCLC [11]. The GPCR signaling is essential for mediating T cell immunity owing to its effects on T cell activation, function, and homeostasis, and a variety of its mediators (including RGS proteins) are involved in T cell-mediated immunity [12]. Interestingly, our bioinformatics analyses revealed high RGS2 expression in $CD8^+$ Tex cells in LC. Furthermore, we identified the basic leucine zipper ATF-like transcription factor 2 (BATF2) as an upstream regulator of RGS2. It has been demonstrated that Tex cells express more BATF, which is essential for the development and maintenance of T cell exhaustion during a chronic infection [13]. The loss of BATF enhances the anti-tumor performance of chimeric antigen receptors T cell therapy (CAR-T) by increasing their resistance to exhaustion and tumor eradication efficacy [14]. Considering the evidence above, we hypothesized that BATF2 might mediate RGS2 expression to control T cell exhaustion in LC, hoping to provide a valuable reference for identifying novel targets for LC treatment and overcoming T cell exhaustion to further improve the efficacy of immunotherapy.

Materials and methods

$CD8^+$ T cell clustering and annotation

The GSE176021 dataset consisted of single-cell data from six patients with NSCLC treated with anti-PD-1 therapy. Poor-quality cells were first filtered out using the "Seurat" package in the R software to ensure the analysis accuracy and exclude cells that may be disturbed by noise or other factors based on follow thresholds: min. cells = 3, min. features = 200, nFeature_RNA < 3000, nCount_RNA< 10000, and percent.mt < 20. Next, the "FindAllmarkers" function was used to calculate the characteristic gene set in the dataset that exhibits high variability between cells. Principal component analysis (PCA) was employed to downscale the high-dimensional data to a lower dimension that was easier to handle. Specifically, we used 40 principal components and a resolution of 0.8 to complete the clustering. For data visualization and the identification of possible cell subpopulations, the uniform manifold approximation and projection (UMAP) and t-distributed stochastic neighbour embedding (t-SNE) methods were also utilized. Finally, the ProjecTIL package was used for the subpopulation annotation of T cells.

Differential analysis of $CD8^+$ Tex and naïve subgroups

Differential gene analysis was implemented on subpopulations of cells in different states using the "FindMarkers" function of the Seurat software package to identify differential genes between $CD8^+$ Tex and naïve subpopulations. We also obtained two datasets GSE218258 and GSE229353 in the GEO database (https://www.ncbi.nlm.nih.gov/geo/) to analyse differentially expressed genes (DEGs) based on "DESeq2" package. Significant differential genes were identified by setting thresholds, including a fold change > 1.5 and a *P*-value < 0.05. Lastly, the ClusterProfiler enrichGO and enrichKEGG functions were used to conduct enrichment analyses for the Kyoto Encyclopedia of Genes and Genomes (KEGG) and Gene Ontology (GO), respectively.

Cellular communication analysis

CellChat is a powerful tool that enables researchers to explore the complexity of intercellular communications and identify potential communication pathways. Intercellular communication was modeled using three modules: a database of cross-referenced ligand-receptor interactions, inference and visualization of intercellular communication, and quantitative analysis of intercellular communication, with CellChatDB.human as the reference database. Interactions among subpopulations of $CD8^+$ T cells were inferred from expression values using the computeCommunProb function. NetVisual_circle was used to display the number of communications

or total communication strength between any two subpopulations.

Single-cell analysis of transcription factors

First, gene regulatory network boosting 2 (GRNBoost2) was employed to establish the regulatory relationships between potential transcription factors and target genes based on the co-expression of genes to identify which transcription factors may regulate which target genes in which subpopulations. Next, the area under the curve for enrichment of gene sets (AUCell) was used to calculate the activity of each transcription factor. Finally, transcription factor activity data were analyzed to identify transcription factors specific to different subpopulations. These subpopulation-specific transcription factors are likely to play key regulatory roles.

Differential analysis of RGS2 high and low expression groups

The Cancer Genome Atlas Lung Adenocarcinoma (TCGA-LUAD) was obtained from UCSC Xena (https://xena.ucsc.edu/) and classified into two groups based on the median expression level of RGS2: a group with high expression of RGS2 and a group with low expression of RGS2. The data preprocessing step involved using the limma package in R to normalize the data and identify genes that were differentially expressed. The normalized data were subjected to an enrichment analysis using the gene set enrichment analysis (GSEA) package. Based on the hallmark gene set in MSigDB 7.0, significantly enriched gene sets were identified at $P< 0.05$.

Correlation between RGS2 expression and immunotherapy

The ESTIMATE algorithm was utilized to examine changes in the abundance of stromal and immune cells between RGS2 high and low groups [15]. The TIDE score (http://tide.dfci.harvard.edu/) is commonly used to assess the predicted response to tumor immunotherapy, and we used it to analyze the relationship between immunotherapy response and RGS2 gene expression [16].

Mice

C57BL/6 mice were obtained from Beijing SLC. The C57BL/6 genetic background was used in breeding both mouse strains, and they were housed in germ-free conditions. The mice were housed in a controlled environment with a 14-h light and 10-h dark cycle at a temperature of 24℃ and a humidity level of 50%. All animal procedures and experimental protocols followed institutional guidelines and had approval from the Animal Research Committee of Zhongda Hospital, School of Medicine, Southeast University (approval NO.20210301085). These procedures were conducted in compliance with regulations stipulated by the National Institutes of Health. This study used male mice that were 8 and 10 weeks old.

Murine primary LC model and murine tumor organoid (MTO) culture

Wild-type (WT), RGS2 knock-out ($RGS2^{-/-}$), or BATF2 knock-out ($BATF2^{-/-}$) mice were housed in a controlled environment at 15~25 °C for 58 h before experimental procedures, with low levels of ambient illumination and minimal acoustic interference. Following the collection of whole blood through the cardiac puncture, C57BL/6 mice were housed for 14 d. Subsequently, a murine LC model was established by intrabronchial injection of methylcholanthrene (MCA) in iodised oil. Briefly, 10 mg of MCA was dissolved in 0.1 mL of iodised oil, achieving homogenisation by incubation at 76~78 °C for 24 h. Part of the fundamental anesthetic regimen involved injecting 0.12 mL of ketamine hydrochloride intramuscularly at 0.6 mL/kg into the right thigh. To prevent potential infections, 20,000 units of penicillin and 50 mg of streptomycin were injected intramuscularly into the left thigh daily for one week.

Mice were sedated at an early stage, approximately 2~3 min after anesthesia, and anaesthetized with diethyl ether to achieve laryngeal muscle relaxation. The anesthetized mice were placed on an inclined platform at 45 °C and maxillary incisors were fixed on the upper end of the platform with retention sutures. The trachea was exposed using an appropriate instrument, and a blunt-tipped injection needle containing a 1 mL syringe was carefully inserted into the glottis during the inspiratory phase. The needle was then directed towards the bronchi of the inferior lobe of the left lung, where 0.1 mL of iodized oil containing 10 mg of MCA was injected. Subsequently, digital subtraction angiography (DSA) was used to capture images and locate the iodized oil infused into the MCA. After 180 d post-installation, the mice were euthanized and systematically dissected to obtain the LC tissues. The tissues were mechanically minced and digested with a solution consisting of collagenase type XI (0.25 mg/mL), dispase (0.1 mg/mL), and 1% fetal bovine serum in Dulbecco's Modified Eagle Medium (DMEM). subsequently, the cellular debris was given time to settle, and the dissociated cells were collected and rinsed with advanced DMEM/F12 before being seeded in Matrigel. Once the Matrigel solidified, the mouse organoid expansion medium was gradually introduced. This medium was based on a foundational mouse organoid basic medium (OBM) that contained B27, N2, N-acetylcysteine, gastrin, EGF, R-spondin-1, FGF10, nicotinamide, and HGF, as well as advanced DMEM/F12, 1% penicillin/streptomycin, and 1% GlutaMAX. For the initial three days

of culture, the medium used to maintain the organoids was supplemented with noggin, Wnt3a, and Y-27632. To re-embed the organoids in the new Matrigel, they were mechanically dissociated into smaller fragments using pipettes after being harvested using a cold OBM medium during passaging. The weekly passage was carried out at 1,6~1,10 following the organoids'growth characteristics. Following traditional protocols, the organoids were passaged and introduced to a freezing medium containing 10% dimethyl sulfoxide and 90% fetal bovine serum to establish a frozen stock. Subsequently, the cultures were thawed, rinsed with OBM, and placed in Matrigel along with organoid initiation media for the initial passaging process.

Immunohistochemistry (IHC)

Paraffin-embedded tissues were sectioned at 5 μm, deparaffinized in xylene, and rehydrated in graded ethanol solutions. Antigen retrieval was performed by immersing the slides in sodium citrate buffer (pH 6.0) or Tris-EDTA buffer (pH 9.0), followed by heating in a microwave oven for 20 min or using a pressure cooker (BioCare Medical) set to 95 °C for 15 min. After cooling, slides were rinsed in distilled water and incubated with 3% hydrogen peroxide for 10 min at room temperature to block endogenous peroxidase activity. Non-specific binding was blocked by incubating sections with 5% bovine serum albumin (BSA; Sigma-Aldrich) or 10% normal goat serum (Vector Laboratories) for 1 h at room temperature. Primary antibodies were diluted in 1% BSA and applied overnight at 4 °C. The following antibodies were used: anti-CD8 (1:200, BioLegend), anti-PD-1 (1:200, Cell Signaling Technology), anti-PD-L1 (1:200, Cell Signaling Technology), anti-CTLA4 (1:200, Abcam), anti-VEGFA (vascular endothelial growth factor A) (1:200, Abcam), anti-FoxP3 (Forkhead Box P3) (1:100, BioLegend), anti-VIM (Vimentin) (1:200, Abcam), and anti-SDF1 (stromal-derived factor 1) (1:200, Cell Signaling Technology). After primary antibody incubation, sections were washed in phosphate-buffered saline (PBS) and incubated with species-specific biotinylated secondary antibodies (1:200, Vector Laboratories) for 1 h at room temperature. Detection was performed using an avidin-biotin complex (ABC) reagent (Vectastain ABC Kit, Vector Laboratories) for 30 min, followed by color development with 3,3'-diaminobenzidine (DAB; Vector Laboratories). Sections were counterstained with Mayer's hematoxylin (Sigma-Aldrich), dehydrated, and mounted using DPX mounting medium. Slides were scanned using an Aperio AT2 digital slide scanner (Leica Biosystems) and analyzed using QuPath software (v.0.3.2). For IHC quantification, five random high-power fields (400× magnification) per tissue section were analyzed. Total cell counts were determined by hematoxylin-stained nuclei, and positive staining for specific markers was quantified. Data represent the mean percentage of positive cells relative to total cells across three biological replicates (n = 3 mice per group), and the positive staining area was quantified using Image J software.

$CD8^+$ T cell collection

A 10^8–10^9 cells/mL suspension of spleen lymphocytes was prepared from WT, $RGS2^{-/-}$, or $BATF2^{-/-}$ mice. Magnet beads were used to sort and purify the $CD3^+$ cells. Subsequently, the single cell suspension was activated using anti-CD3 (2 μg/mL) and anti-CD28 (2 μg/mL) antibodies (eBioscience) for 48 h in RPMI-1640 medium supplemented with 10% fetal bovine serum, 2 mM L-glutamine, and 1% penicillin/streptomycin to collect $CD8^+$ T cells. After stimulation, the $CD8^+$ T cells ($CD45^+CD3^+CD8^+$) were identified by flow cytometry

Fluorescence-activated cell sorting (FACS)

Flow cytometry was conducted on the cells of the tumor tissue. These tumor-infiltrating cells were derived from primary tumors in wild-type (WT), RGS2 knock-out ($RGS2^{-/-}$) mice that underwent orthotopic tumor organ transplantation in lung and metastatic liver tumors. Fresh tumor samples were enzymatically separated to produce tumor-infiltrating cells using a tumor dissociation kit (130-096–730; Miltenyi Biotec). Red blood cells were then removed using a Red Blood Cell Lysis Solution (130-094–183; Miltenyi Biotec). The isolated cells were first blocked for 10 min on ice using a mouse Fc Block (1,50, anti-CD16/CD32 antibody; 553142, BD Biosciences). A 30-min ice incubation with the appropriate antibodies followed this. Fixation and permeabilization methods were used for intracellular staining, with the transcription factor buffer set (562574; BD Biosciences). Subsequently, the cells were incubated for an additional 30-min incubation period. FlowJo V10 was used to analyze the data after flow cytometry analysis was completed using a FACSAria II device (BD Biosciences). After gating on live, single cells (FSC/SSC and FSC-H/FSC-A), $CD45^+$ leukocytes were selected, followed by gating on $CD3^+$ T cells to obtain the T cell population. $CD8^+$ T cell subsets were then sorted and further characterized by the expression of PD-1 ($CD8^+PD\text{-}1^+$), CD69 ($CD8^+CD69^+$), interferon-gamma (IFNγ) ($CD8^+IFN\gamma^+$), T-Cell Factor 7 (TCF7) ($CD8^+TCF7^+$), CTLA4 ($CD8^+CTLA4^+$), and T-Cell Immunoglobulin and Mucin-Domain Containing-3 (TIM-3) ($CD8^+TIM3^+$) to assess activation and exhaustion markers. Regulatory T cells (Tregs) were identified as $CD3^+CD4^+CD25^+Foxp3^+$. Dendritic cells (DCs) were selected as $CD11c^+CD86^+MHCII^+$, and myeloid-derived suppressor cells (MDSC) as $CD11b^+Ly6G^+$

(polymorphonuclear MDSCs). Proper compensation and isotype controls were applied, and data were analyzed using FlowJo V10. The gating strategy is exhibited in Supplementary File 1.

Cell culture and treatment

Short hairpin RNAs (shRNAs) targeting RGS2 and BATF2 were designed using an online shRNA design tool, with sequences selected for optimal knockdown efficiency and minimal off-target effects. The shRNA oligonucleotides were annealed and cloned into the pLKO.1 lentiviral vector using AgeI and EcoRI restriction sites, and the constructs were verified by Sanger sequencing. Lentiviral particles were generated by co-transfecting HEK293 T cells with the shRNA-containing pLKO.1 vector, psPAX2 (packaging plasmid), and pMD2.G (envelope plasmid) at a 4:3:1 ratio using Lipofectamine 3000 (Thermo Fisher Scientific). After 48 h, viral supernatants were harvested, filtered through a 0.45-μm filter, and concentrated by ultracentrifugation at 25,000× *g* for 2 h at 4℃. Target cells (A549 and H1299) were seeded in six-well plates (3×10^5 cells per well) and transduced with lentiviral particles in the presence of 8 μg/mL polybrene. After 24 h, the medium was replaced, and cells were cultured for an additional 48 h before selection with 2 μg/mL puromycin for 5 d to establish stable knockdown cell lines. Knockdown efficiency was validated by RNA extraction and real time-quantitative polymerase chain reaction (RT-qPCR) using primers specific to RGS2 and BATF2, with glyceraldehyde-3-phosphate dehydrogenase (GAPDH) as an internal control, and by Western blot (WB) analysis to confirm protein level reduction. Functional assays, including colony formation and 5-Ethynyl-2'-deoxyuridine (EdU) labelling assays, were performed to assess cell proliferation, while co-culture experiments with mouse-derived T cells were used to evaluate immune modulation, such as cytokine production (interleukin-2 [IL-2], IFN-γ, and granzyme B [GZMB]) and exhaustion marker expression (PD-1, TIM3, and CTLA4).

WB analysis

Tumor tissue was lysed using a pre-chilled radioimmune precipitation assay (RIPA) buffer, which included a protease inhibitor cocktail (Roche) and a phosphatase inhibitor mixture (Thermo Fisher Scientific). The buffer contained 50 mM Tris, pH 7.4, 150 mM NaCl, 1% Nonidet P-40, 0.5% sodium deoxycholate, and 0.1% sodium dodecyl sulfate. A bicinchoninic acid (BCA) kit from Thermo Fisher Scientific was used to measure the protein concentration in the cell lysates. Each sample's cell lysate was used in twenty micrograms for the polyacrylamide gel electrophoresis. Proteins were transferred onto PVDF (polyvinylidene fluoride) membranes, which were then blocked for the next 24 h with 5% non-fat milk and incubated for 2 h at room temperature with primary antibodies. Following a three-step washing process, the membrane was incubated with horseradish peroxidase-conjugated with secondary antibodies anti-mouse or anti-rabbit for 1.5 h at a 1:500 ratio. Subsequently, the membrane was washed again and then exposed to chemiluminescent substrates from the Western Lightning Plus ECL kit (PerkinElmer) before being visualized using X-ray film for image analysis. Protein band intensities were quantified using ImageJ software and normalized to the loading control (GAPDH). The antibodies used are exhibited in Table 1.

RT-qPCR

Thermo Fisher Scientific's miRNeasy mini kit (Qiagen, 157029493) was used to purify the total RNA collected from the cells using TRIzol (260808, Ambion). We used a NanoDrop 2000 spectrophotometer to measure the quantity and quality of RNA. Using the qscriptXLT cDNA superMix reagent (Quantabio, 66141329), 1 μg of RNA was reverse transcribed for cDNA synthesis. This was followed by qPCR using a QuantStudio real-time PCR system (Thermo Fisher Scientific) with the SYBR Green FastMix Low ROX reagent (TaKaRa). The primers for each mRNA are exhibited in Table 2. Relative mRNA expression, normalized to the loading control (GAPDH), was examined using the $2^{-\Delta\Delta Ct}$ method.

Enzyme-linked immunosorbent assay (ELISA)

The levels of interleukin-2 (IL-2), interferon-gamma (IFN-γ), granzyme B (GZMB), and tumor necrosis factor-alpha (TNF-α) were measured in the serum and/or tumor tissue homogenates of tumor-bearing mice. After euthanizing the mice, blood samples were collected by cardiac puncture and centrifuged at 4℃ to obtain serum. Tumor tissue samples were harvested, weighed, and homogenized in an appropriate lysis buffer to extract proteins, following the manufacturer's protocol. The concentration of each cytokine was determined using commercially available ELISA kits specific for IL-2, IFN-γ, GZMB, and TNF-α (all purchased from Thermo Fisher Scientific) following the manufacturer's instructions. Briefly, 96-well plates were coated with capture antibodies specific for each cytokine overnight at 4℃. After blocking the wells with a blocking buffer, serum or homogenized tumor tissue supernatants were added to the wells and incubated for 2 h at room temperature. After washing, the detection antibody was added, followed by incubation for 1 h. A substrate solution was then added, and the color change was measured using a microplate reader at 450 nm to quantify cytokine levels. The concentration of each

Table 1 Antibodies

Symbol	Catalog	Company	Dilution	Validation
RGS2	Ab36561	ABCAM	1 μg/ml	Not applicable
BATF2	PA5-37,138	ThermoFisher	1:1000	Not applicable
CD8	14–0808-82	ThermoFisher	0.25 μg/test Or 5 μg/mL	Relative expression
PD1	AB214421	ABCAM	1:1000	Not applicable
PDL1	14–5982-82	ThermoFisher	1:500 or 0.25 μg/test	Cell treatment
TIM3	83,882	CST	1:100	Not applicable
CTLA4	GTX639560	Genetex	1:1000	Orthogonal Validation
CD14	93,882	CST	1:250	Not applicable
CD33	GTX01852	Genetex	1:1000	Not applicable
VEGFA	GTX637405	Genetex	1:1000	Orthogonal Validation
CD31	77,699	CST	1:200	Not applicable
VIM1	5741	CST	1:100	Not applicable
SDF1	GTX116092	Genetex	1:3000	Orthogonal Validation
IkKα	GTX132964	Genetex	1:2000	validation
phos-IkKα	GTX17943	Genetex	1:2000	Orthogonal Validation
p65	Ab32536	ABCAM	1:3000	KO validation
phos-p65	Ab76302	ABCAM	1:3000	Not applicable
JNK	66,210–1-Ig	proteintech	1:3000	KO validation
phos-JNK	80,024–1-RR	proteintech	1:3000	Not applicable
p38	14,064–1-AP	proteintech	1:2000	KO validation
phos-p38	28,796–1-AP	proteintech	1:2000	Not applicable
LAG3	16,616–1-AP	proteintech	1:500	Not applicable
CD38	GTX03746	Genetex	1:50	Not applicable
2B4	54,560	CST	1:1000	Not applicable
TBX21	GTX31554	Genetex	1:1000	Not applicable
TCF7	14,464–1-AP	proteintech	1:1000	KO validation
CD122	GTX53197	Genetex	1:1000	Not applicable
CD127	17,626–1-AP	Proteintech	1:1000	Not applicable
CD45RA	PA5-87,427	ThermoFisher	1:1000	Not applicable
CCR7	MA1-163	ThermoFisher	1:1000	Not applicable
GZMB	GTX81831	Genetex	1:50	Not applicable
VISTA	54,979	CST	1:300	Not applicable
GAPDH	GTX100118	Genetex	1:5000	Orthogonal Validation
C-CAS3	Ab184787	ABCAM	1:1000	KO validation
CD206	Ab64693	ABCAM	0.5 μg/ml	Not applicable
CD36	Ab252922	ABCAM	1:1000	Not applicable

cytokine was calculated from a standard curve generated using known concentrations of recombinant cytokines provided in the kits.

Colony formation assays

In six-well plates, LUAD cells were seeded at a density of 1×10^3 cells/well and treated with CO_2 for 48 h at 37 °C. After incubation for 14 d with the medium refreshed every 2–3 d, PBS was used to wash the clones twice before they were preserved in distilled water with 2% formaldehyde and 10% methanol. Staining agents used on the colonies included 0.5% crystal violet/20% methanol/PBS. The number of colonies was measured with Oxford Optronix-GELCOUNT.

EdU labeling assay

Cells were resuspended in 500 ul and seeded into a 24-well plate at a ratio of 2×10^4 cells per well and 300 μL of medium containing 50 μM of EdU reagent (RiboBio Biotechnology, Guangzhou, China) was added. The

Table 2 Primers for qPCR analysis

Symbol		Sequences
RGS2	Forward	GCGGGAGAAAATGAAGCGGACA
	Reverse	TCTTGCCAGTTTTGGGCTTCCC
BATF2	Forward	GAAGCAGAAGAACCGAGTGGCT
	Reverse	TGCCAGCTCAGTCTGCAAGGC
LAG3	Forward	CTCCATCACGTACAACCTCAAGG
	Reverse	GGAGTCCACTTGGCAATGAGCA
CD38	Forward	GGTCCAAGTGATGCTCAATGGG
	Reverse	AGCTCCTTCGATGTCGTGCATC
2B4	Forward	CAGTTGCCACAGCAGACTTTCC
	Reverse	CTTCCTGGAAGGCTGGACTACT
TBX21	Forward	CCACCTGTTGTGGTCCAAGTTC
	Reverse	CCACAAACATCCTGTAATGGCTTG
TCF7	Forward	CCTGCGGATATAGACAGCACTTC
	Reverse	TGTCCAGGTACACCAGATCCCA
CD122	Forward	GGTGGAACCAAACCTGTGAGCT
	Reverse	GGTGACGATGTCAACTGTGGTC
CD127	Forward	CACAGCCAGTTGGAAGTGGATG
	Reverse	GGCATTTCACTCGTAAAAGAGCC
CD45RA	Forward	CTTCAGTGGTCCCATTGTGGTG
	Reverse	TCAGACACCTCTGTCGCCTTAG
CCR7	Forward	AGAGGCTCAAGACCATGACGGA
	Reverse	TCCAGGACTTGGCTTCGCTGTA
TIM3	Forward	ACAGACACTGGTGACCCTCCAT
	Reverse	CAGCAGAGACTCCCACTCCAAT
CTLA4	Forward	GTACCTCTGCAAGGTGGAACTC
	Reverse	CCAAAGGAGGAAGTCAGAATCCG
CXCL13	Forward	CATAGATCGGATTCAAGTTACGCC
	Reverse	GTAACCATTTGGCACGAGGATTC
PD-1	Forward	AAGGCGCAGATCAAAGAGAGCC
	Reverse	CAACCACCAGGGTTTGGAACTG
CD8	Forward	ACTACCAAGCCAGTGCTGCGAA
	Reverse	ATCACAGGCGAAGTCCAATCCG
GAPDH	Forward	CATCACTGCCACCCAGAAGACTG
	Reverse	ATGCCAGTGAGCTTCCCGTTCAG

wells were then incubated for 2 hours in a cell incubator. Remove the EdU medium and wash the cells with PBS two times for 5 min each. Subsequently, the cells were permeabilized with 0.5% Triton X-100 for 10 min, quenched in glycine solution (2 mg/mL), fixed with 4% paraformaldehyde in PBS for 30 min at room temperature, then stained for 30 min with Apollo dye solution. A charge-coupled device (CCD) camera was used to take pictures with the Zeiss OBSERVER D1/AX10 cam HRC microscope (Oberkochen, Germany).

Luciferase assay

The promoter sequence of RGS2 was inserted into the pGL3-Luc vector (Promega, Guangzhou, China) to construct the promoter luciferase reporter vector of RGS2. Following a 48-h incubation period, the luciferase activity was assessed using the Dual-Luciferase Reporter Gene Assay System (Promega, USA) on 293 T cells (Promoter) co-transfected with either Emp or BATF.

Statistical analyses

Two-group comparisons were performed using the Student's t-test; multi-group comparisons were performed using either a one- or two-way analysis of variance (ANOVA). The data was shown as mean ± standard deviation (SD). After at least three separate rounds of each experiment, similar results were obtained, and representative pictures were obtained. For the correlation study between two continuous variables, Pearson's correlation coefficient (r) was utilized, and Pearson's correlation test was employed to calculate p-values. The Kaplan-Meier method was used to create the survival curves, and the log-rank test was used to compare them. GraphPad V9.0 was used for statistical analysis, and two-tailed statistical tests were used in all of the tests.

Results

High RGS2 levels predict poor outcomes and reduced benefit from PD-1/PD-L1 blockade therapy

In this study, data from 6 patients who received neoadjuvant PD-1 blockade therapy were retrieved from the GSE176021 dataset. $CD8^+$ T cells were clustered and subgrouped by PCA and UMAP downscaling with a resolution of 0.3 using the FindClusters function in Seurat. Based on the ProjecTILs algorithm results, T cells were categorized into a total of 9 subpopulations (Fig. 1A), of which CD8.EarlyActive, CD8. Naïve, and CD8. Tex were predominant (Fig. 1B). The Seurat and Wilcoxon rank-sum tests' FindAllMarkers function was used to identify marker genes for each subpopulation (Fig. 1C). Next, a co-expression matrix was constructed using the hdWGCNA algorithm. To ensure an unsigned scale-free network, the co-expression similarity matrix was transformed into a neighbor-joining matrix using a best soft-power of $\beta = 7$ (Fig. 1D). The metacells were subsequently classified into 7 modules based on the topological overlap matrix (unclassified metacells in gray) (Fig. 1E). Each co-expression module was displayed on a UMP downscaling map. The blue module was significantly enriched in the $CD8^+$ Tex cells (Fig. 1F). We plotted dot plots of the correlation of co-expression modules with cell subpopulations, with the blue module being most correlated with CD8.Tex (Fig. 1G). The correlation network of core genes within the blue module was mapped and the top 10 hub

genes were identified by the MCC algorithm (Fig. 1H-I). The function FindMarkers was used to filter genes that were differentially expressed (DEGs) between $CD8^+$ Tex and $CD8^+$ Naïve cells (Fig. 1J). We also obtained DEGs in GSE218258 (four patients with LC) and GSE229353 (seven patients with NSCLC treated with anti-PD-1 therapy) (Fig. 1K-L). Subsequently, an intersection analysis was performed in DEGs from GSE218258, GSE229353, GSE176021, and the blue module Top10 genes, resulting in an identification of three shared genes were most associated with CD8.Tex cells based on the results of the blue module and the difference analysis of the three datasets (Fig. 1M). These genes are NEU1, CACYBP and RGS2 (Fig. 1N). The DEGs from two datasets (GSE218258 and GSE229353) mainly regulated hematopoiesis and leukocyte differentiation (Fig. 1O) and were significantly enriched in the NF-κB pathway (Fig. 1P).

The expression differences of key genes between major pathologic response (MPR) and non-MPR patients were plotted. There was no significant difference in the expression level of CACYBP between MPR and non-MPR patients, but NEU1 and RGS2 were significantly up-regulated in MPR patients (Fig. 2A). In the TCGA database, RGS2 was significantly upregulated in LUAD paracancer samples, but NEU1 and CACYBP showed non-significant changes between cancer and paracancer samples (Fig. 2B). In addition, survival analysis showed that both CACYBP and RGS2 were significant risk factors for disease-free survival in LUAD patients (Fig. 2C). Therefore, RGS2 was selected for further analyses. A total of 4,264 RGS2-associated DEGs were identified in the TCGA-LUAD database (Fig. 2D). These genes are mainly involved in signal release, membrane potential regulation, and neuroactive ligand-receptor interactions (Fig. 2E-F). GSEA showed that high expression of RGS2 activated allograft rejection, TNF-a signaling via NF-κB, and inflammatory response (Fig. 2G). Using the AUCell algorithm, we found that the TNF-a signalling via the NF-κB metabolic pathway was significantly active in $CD8^+$ Tex cells in patients with MPR following anti-PD-1 treatment (Fig. 2H). High expression of RGS2 was accompanied by a higher abundance of stromal and immune cells rather than low expression of RGS2 (Fig. 2I). The TIDE scores showed that the response rate of high RGS2 expression (83.0%) was markedly higher than that of low RGS2 expression (36.0%) (Fig. 2J). Our previous analysis showed that RGS2 was highly expressed in Tex. Reducing RGS2 expression may help restore the functionality of exhausted T cells, allowing them to regain their ability to proliferate, produce cytokines, and perform cytotoxic functions.

Inhibition of RGS2 suppresses inflammation and immunosuppression in aggressive murine LC

3LL cells were inoculated into $RGS2^{-/-}$ mice via tail vein injection (Fig. 3A). In $RGS2^{-/-}$ mice, RGS2 expression was nearly undetectable in $CD8^+$ T cells, as confirmed by immunofluorescence staining (Fig. S1 A). Knock-out of RGS2 significantly reduced the number of metastatic nodules formed by 3LL cells in both lung tissues (Fig. 3B) and liver tissues (Fig. 3C), suppressed SDF1- or VIM1-positive cells in metastatic nodules formed by 3LL cells (Fig. 3D-E). Similarly, lower SDF1 and VEGFA levels (Fig. 3F-G) reflect impaired angiogenesis and reduced stromal support for metastatic tumor growth, contributing to the diminished metastatic burden observed in $RGS2^{-/-}$ mice. Furthermore, IHC analysis showed that knock-out of RGS2 in mice resulted in a significant reduction in classical markers of T cell exhaustion (PD-1, CTLA4, and TIM3) (Fig. 3H-I). These findings, combined with the association of RGS2 with exhaustion-related pathways, support the hypothesis that RGS2 contributes to T cell exhaustion within the TME. Besides, the CD8 specific cytokines TNFA, IL-2, IFN-γ, and GZMB were upregulated in $RGS2^{-/-}$ mice (Fig. S1B-C). Thus, we extracted T cells from the mouse spleen and induced them with CD3/CD28 (Fig. 3J). Compared to those extracted from WT mice, the T cells extracted from $RGS2^{-/-}$ mice showed significantly increased activation, as manifested by reduced levels of the T cell

(See figure on next page.)

Fig. 1 RGS2 plays a crucial role in $CD8^+$ Tex cells. **A** T cell clustering and subgrouping; cells are assigned into 9 subgroups. **B** Proportion of T cell subgroups. **C** Expression of marker genes in T cell subgroups. **D** Choosing the optimal soft threshold parameter for transforming the co-expression similarity matrix into an adjacency matrix. **E** Single-cell WGCNA gene expression hierarchical clustering. **F** UMAP dimensionality reduction plot showing the gene expression levels in co-expression modules in $CD8^+$ T cell subgroups. **G** The blue module has the strongest connection with Tex in the Bubble Chart, depicting the correlation between each co-expression module and T cell subsets. **H** Co-expression network of gene sets within the blue module. **I** MCC algorithm selects the top 10 genes from the blue module. **J** A volcano plot is showing the genes that $CD8^+$ Tex and naïve $CD8^+$ cells express differently in GSE176021. **K** The GSE218258 dataset's volcano plot displays the genes that exhibit differential expression. **L** The GSE229353 dataset's volcano plot of differentially expressed genes. **M** Intersection of 3 datasets, GSE218258, GSE229353, and GSE176021, with the top 10 genes from the blue module, resulting in three genes, NEU1, CACYBP, and RGS2. **N** Expression of NEU1, CACYBP, and RGS2 genes in $CD8^+$ Tex vs naïve $CD8^+$ T cells. **O** GO enrichment analysis of genes with variable expression. **P** KEGG enrichment analysis of genes that exhibit differential expression

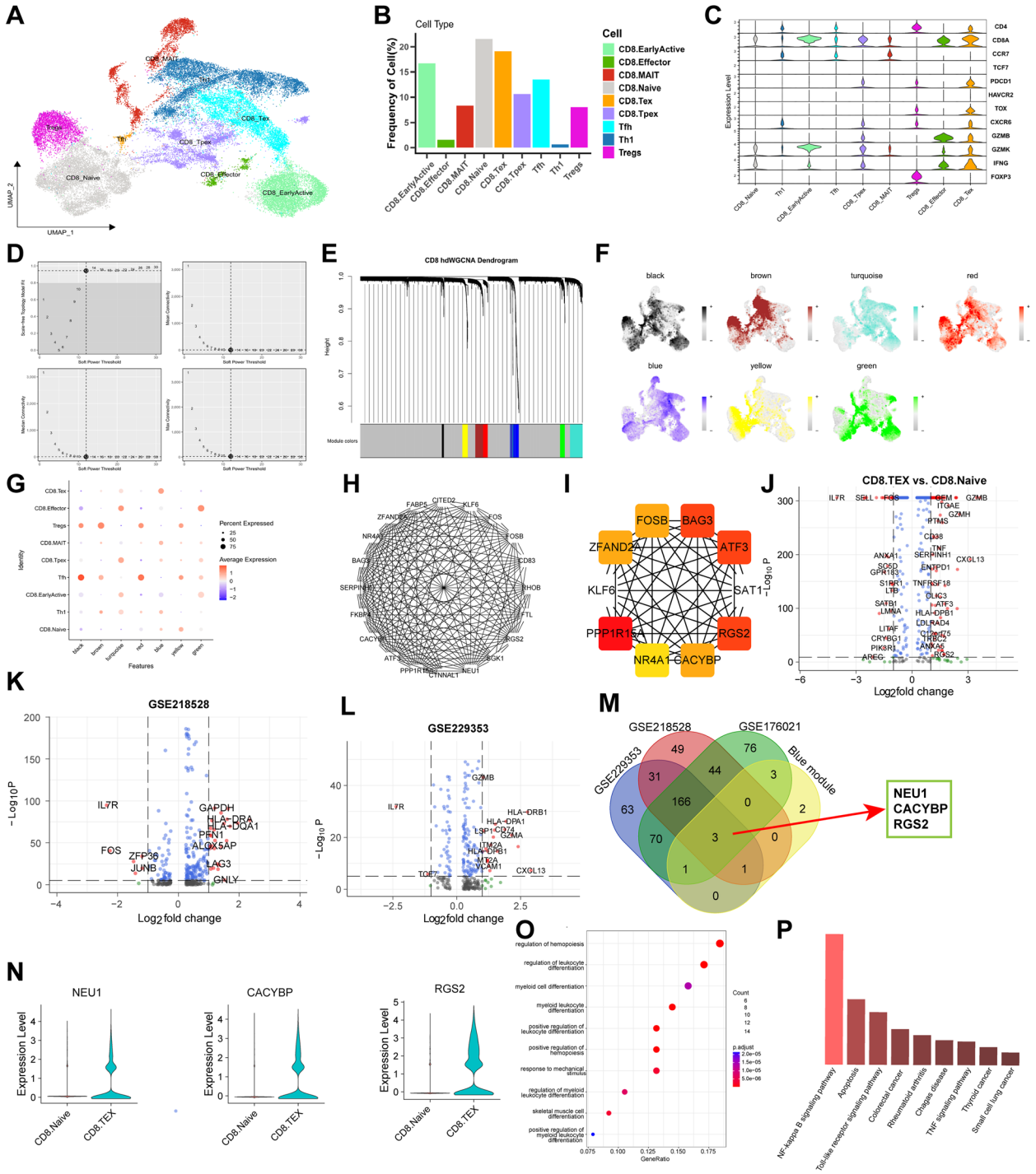

Fig. 1 (See legend on previous page.)

dysfunction markers PD-1, CTLA4 and TIM3 (Fig. 3K). Additionally, a significant increase was observed in the levels of IL-2, IFN-γ, GZMB, and TNFA in the serum of the mice (Fig. 3L). These findings demonstrate that RGS2 supports a pro-tumorigenic TME by promoting angiogenesis, immune cell recruitment, and metastatic niche formation. The absence of RGS2 disrupts these processes, resulting in reduced metastatic burden and improved immune function, as evidenced by increased $CD8^+$ T cell activity.

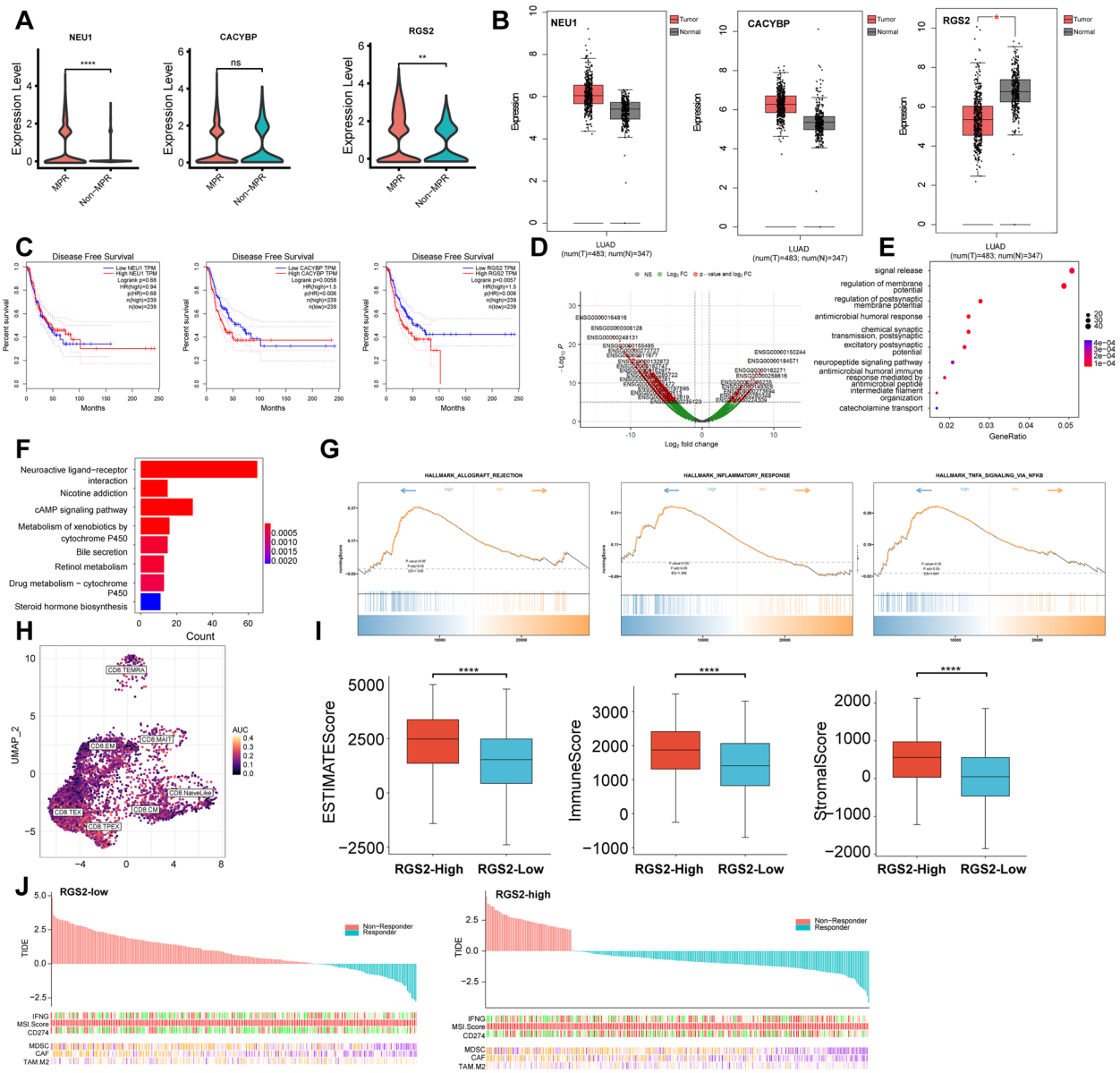

Fig. 2 High RGS2 levels predict poor outcomes and less benefit from PD-1/PD-L1 blockade therapy. **A** Differential expression of NEU1, CACYBP, and RGS2 between MPR and Non-MPR patients. **B** The TCGA database was used to analyze the expression of NEU1, CACYBP, and RGS2 in tumor and surrounding non-tumor tissues. **C** Gene survival analysis of NEU1, CACYBP, and RGS2. **D** A volcano plot showing the genes that differ in expression between the RGS2 high and low expression groups. **E** GO enrichment analysis of DEGs. **F** KEGG enrichment analysis of of DEGs. **G** Genes with differential expression: GSEA enrichment analysis. **H** Expression of the TNFA SIGNALING VIA NFKB pathway in MPR patients after anti-PD-1 treatment analyzed using the AUCell algorithm. **I** Correlation of RGS2 expression levels with ESTIMATE score, Immune score, and Stromal score studied using the ESTIMATE algorithm. **J** Relationship between the high and low expression levels of RGS2 and immunotherapy response

RGS2 facilitates LC progression through immunosuppression within the TME

Murine Tumor Organoids (MTOs) derived from murine lung cancer tissues were labeled with GFP and injected into the upper lobe of the right lung in RGS2$^{-/-}$ and WT mice (Fig. 4A). The growth and metastasis of MTO were significantly inhibited in RGS2$^{-/-}$ mice. Whether in the presence of MTO transplantation or not, the representative images of lungs from WT and RGS2$^{-/-}$ mice showed no significant differences in gross morphology or weight (Fig. 4B). Following the direct injection of MTO-GFP tumor cells into the lung, we observed metastases to the

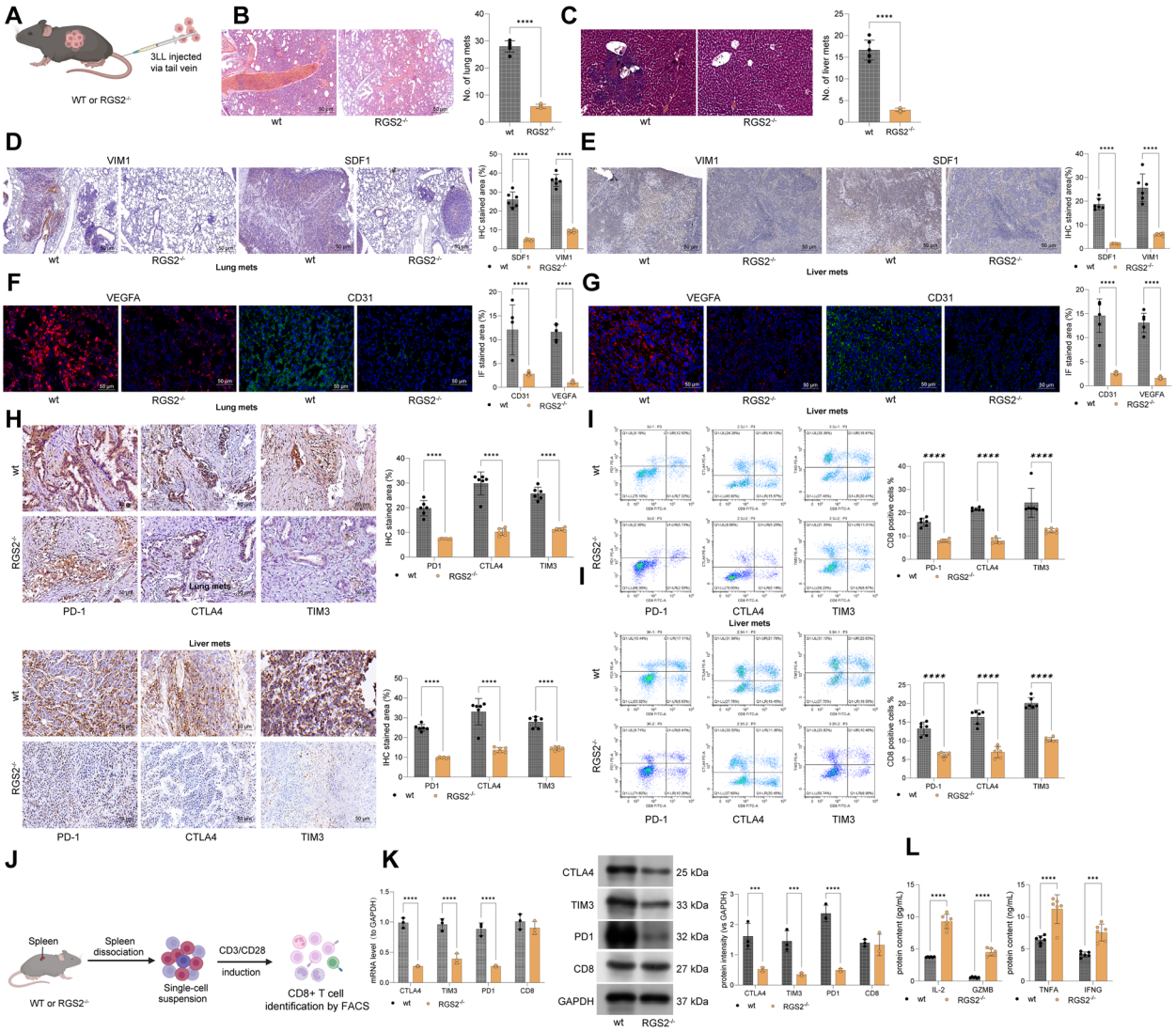

Fig. 3 Inhibition of RGS2 suppresses inflammation and immunosurveillance in aggressive murine LC. **A** Schematic diagram for animal treatment: mouse 3LL cells were injected into WT or RGS2$^{-/-}$ mice through the tail vein. **B**-**C** The number of metastatic foci that 3LL formed metastatic nodules in the mice's lung and liver tissues determined using HE staining. **D**-**E** IHC was used to determine the staining intensities of VIM and SDF1 in the metastatic nodules in the lung and liver tissues. **F**-**G** Immunofluorescence staining to measure the staining intensity of VEGFA and CD31 in mouse lung and liver tissues. **H** IHC to measure the positive staining intensity for PD-1, CTLA4, and TIM-3 in lung and liver tissues; I, FACS to analyze the populations of CD8$^+$PD-1$^+$, CD8$^+$CTLA4$^+$, and CD8$^+$TIM3$^+$ cells in the mouse lung and liver tissues. **J** Schematic diagram of the isolation of spleen lymphocytes from WT or RGS2$^{-/-}$ mice and stimulation of CD3/CD28 antibodies to induce T cells. **K** RT-qPCR and WB to detect the levels of CTLA4, TCF7, PD-1, and CD8 in T cells. **L** ELISA to measure the quantities of cytokines released by T cells. Each dot represents one independent experiment or data from one animal. ****$P < 0.0001$

liver and mediastinal lymph nodes. These metastases were substantially weakened in RGS2$^{-/-}$ mice. (Fig. 4C-D). Phosphorylation levels of p65, JNK and p38 levels were visibly reduced in primary or metastatic tumors of RGS2$^{-/-}$ mice (Fig. 4E-F), and the number of infiltrating CD206$^+$Ly6 C$^+$ cells in tumor tissues were significantly reduced in these mice (Fig. 4G-H). Moreover, the staining intensities of PD-1, PD-L1, and T exhaustion markers CTLA4 and Galectin-9 in tumor tissues were greatly reduced in RGS2$^{-/-}$ mice (Fig 4I-J). Additionally, immunofluorescence staining showed that the positive staining of the T effector GZMB$^+$ was increased while the T cell dysfunction marker VISTA$^+$ was significantly reduced in both primary and metastatic tumor tissues in RGS2$^{-/-}$ mice (Fig. 4K-L). The survival of mice was notably increased upon RGS2 knock-out (Fig. 4M). Additionally, the CD8$^+$ T cells from RGS2$^{-/-}$ mice exhibited significantly reduced expression of exhaustion markers

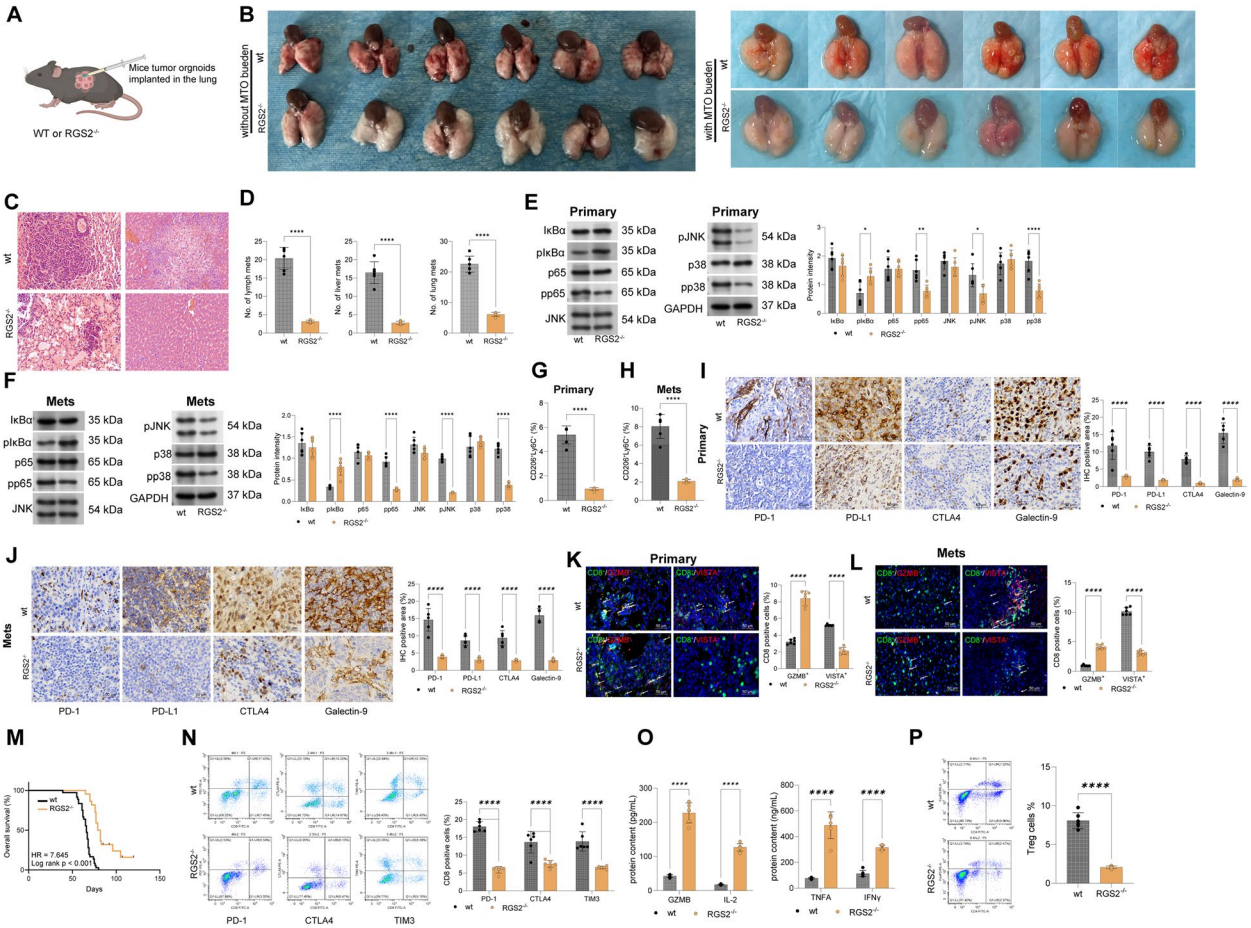

Fig. 4 RGS2 facilitates the progression of lung cancer through immunosuppression in the tumor microenvironment. **A** Schematic representation of MTO injection into WT or RGS2$^{-/-}$ mice. **B** Gross images of the lung tissues and WT or RGS2$^{-/-}$ mice RGS2 with or without MTO burden. **C** tumor burden in lung tissues determined using HE staining. **D** number of lymph node metastasis, liver metastasis, and lung metastasis in mice. **E–F** WB analysis to detect the levels of phosphorylation of IκBα, p65 JUN, and p38, IKKBKB and p65 in primary and liver metastatic nodules of mice. **G-H** FACS to detect the number of CD206^{+}Ly6 C^{+} cells infiltrated in primary and liver metastatic nodules. **I-J** IHC to detect the staining intensity of PD-1, PD-L1, CTLA4, Galectin-9 in primary and liver metastatic nodules. **K-L** Immunofluorescence staining to confirm the number and distribution of CD8^{+}GZMB^{+} or CD8^{+}VISTA^{+} in metastatic primary and liver metastatic nodules. **M** Kaplan–Meier analysis of the mouse survival cycle. Each dot represents one independent experiment or data from one animal. *$P < 0.05$, **$P < 0.01$, and ****$P < 0.0001$

(PD-1, TIM3, CTLA4) and increased production of effector cytokines (IL-2, IFN-γ, GZMB, and TNFA) compared to WT mice (Fig. 4N-O). Additionally, Treg frequencies were reduced in RGS2$^{-/-}$ mice (Fig. 4P). These findings suggest that RGS2 deficiency reprograms the tumor immune microenvironment, enhancing effector T cell activity and reducing immunosuppressive cell populations.

Furthermore, in a mouse model of MCA-induced primary LC, the RGS2 levels were found to be elevated in tumor tissues compared to normal tissues, which were further elevated in metastatic tissues compared to primary tumor tissues (Fig. S2 A-D). Additionally, the TCGA data also suggested that high RGS2 expression was linked to increased liver and lymph node metastasis in LC patients (Fig. S2E-F). According to a Kaplan–Meier survival analysis, patients with LC who had higher RGS2 levels had a poorer prognosis (Fig. S2G).

RGS2 is regulated by BATF2

To confirm the regulation of RGS2 by BATF2, we initially constructed pGL3 luciferase reporter vectors that included either mutant (pGL3-Luc-mt) or wild-type (pGL3-Luc-wt) RGS2 promoter sequences (Fig. 5A). These vectors were co-transfected with BATF2 overexpression plasmids into HEK293 T cells. The BATF2 overexpression plasmid significantly increased the luciferase activity of the pGL3-Luc-wt reporter while having

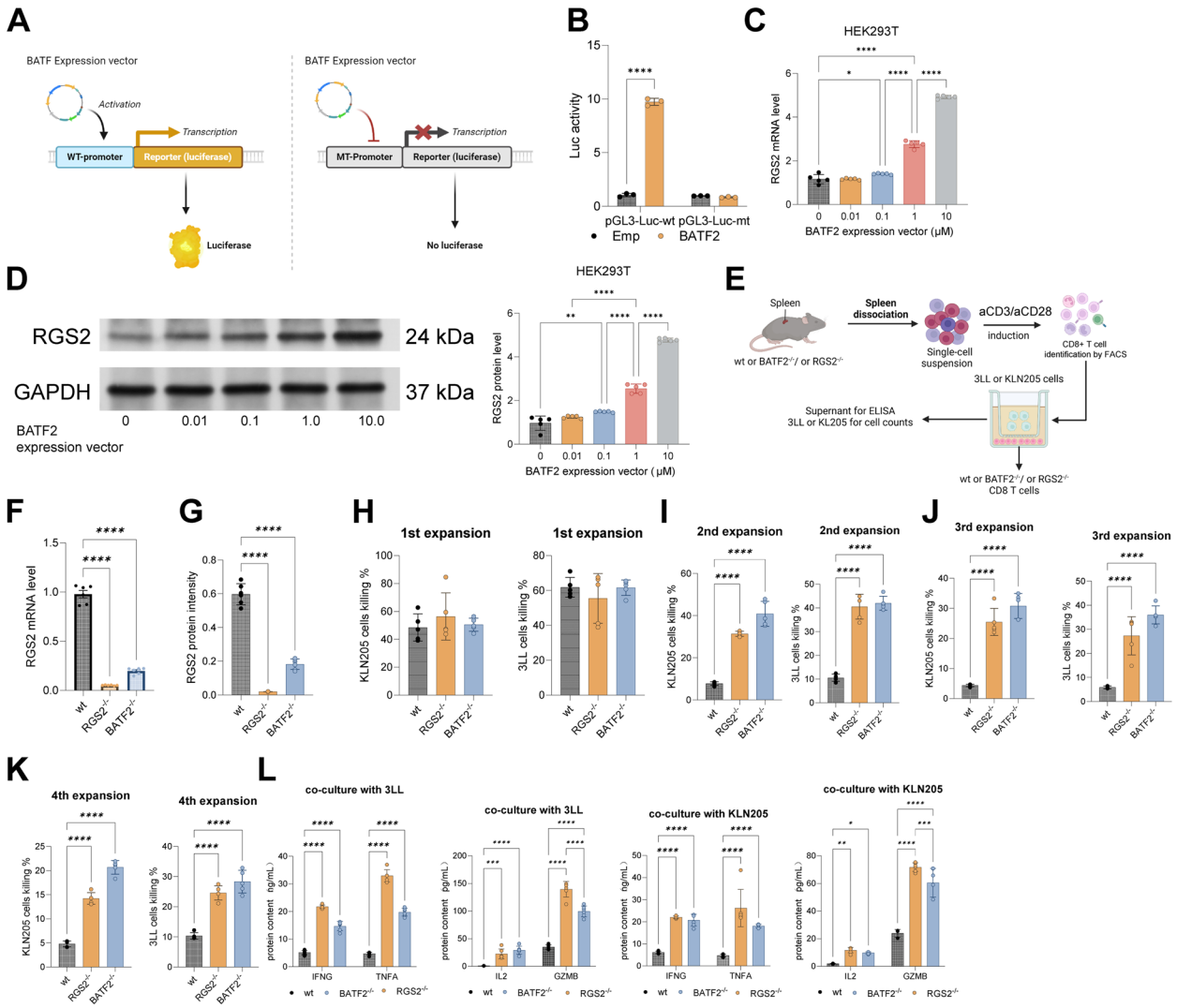

Fig. 5 RGS2 is regulated by BATF. **A** Schematic diagram of the pGL3 luciferase reporter vectors that include the wild-type (wt) RGS2 promoter sequence, as well as the mutant vector. **B** The luciferase reporter assay validates the influence of BATF2 on the transcriptional activity of the luciferase vectors. **C-D** HEK293 T cells were transfected with BATF2 overexpression plasmids at different concentrations, followed by detection of RGS2 mRNA and protein levels. **E** Schematic diagram of the isolation of spleen lymphocytes from WT, RGS2$^{-/-}$, or BALF$^{-/-}$ mice and stimulation of CD3/CD28 antibodies to induce CD8^{+} T cells. These stimulated CD8^{+} T cells were co-cultured with mouse LC cell lines 3LL and KLN205 in Transwell systems. **F-G** mRNA and protein levels of RGS2 in CD8^{+} T cells isolated from WT, RGS2$^{-/-}$, or BALF$^{-/-}$ mice. **H–K** CD8^{+} T cells were co-cultured with 3LL and KLN205 at an E:T = 10:1, and the tumor cell killing rates in 1 st-4 th expansion were analyzed. **L** ELISA to measure the contents of cytokines (IL-2, IFN-γ, GZMB, and TNFA) released by T cells. Each dot represents one independent experiment or data from one animal. *$P < 0.05$, **$P < 0.01$, ***$P < 0.001$, ****$P < 0.0001$

little impact on the pGL3-Luc-mt reporter (Fig. 5B), indicating that BATF2 can bind to the RGS2 promoter sequence. Subsequently, to further verify their regulatory relationship, we transfected BATF2 overexpression plasmids into HEK293 T cells at increasing gradient concentrations. Importantly, the mRNA and protein levels of RGS2 were increased as the BATF2 overexpression plasmid increased (Fig. 5C-D). Additionally, we generated BATF2$^{-/-}$ mice and obtained the CD8^{+} T cells after stimulation with CD3/CD28 antibodies for 48 h (Fig. 5E). A significant reduction in RGS2 levels was detected in the cells extracted from BATF2$^{-/-}$ mice (Fig. 5F-G), indicating that BATF2 regulates RGS2 expression in T cells. Additionally, to confirm whether the BATF2-RGS2 axis influences T cell exhaustion and immune activity, a co-culture experiment was conducted using the extracted T cells with mouse lung cancer cell lines 3LL and KLN205 at an effector-to-target (E:T) ratio of 10:1, as shown in Fig. 5E.

It was observed that T cells extracted from BATF2$^{-/-}$ or RGS2$^{-/-}$ mice exhibited significantly enhanced cytotoxicity against cancer cells in the second to fourth generations, during which T cells were re-exposed to fresh tumor cells every 24 h to evaluate their sustained cytotoxicity over multiple rounds of tumor cell exposure (Fig. 5H-K). Additionally, ELISA assays were performed on supernatants collected after the 2nd expansion (48 h after co-culture) to analyze the production of T cell effector cytokines (IL-2, IFN-γ, GZMB, and TNFA). It was found that the secretion of these cytokines was significantly increased in T cells extracted from BATF2$^{-/-}$ or RGS2$^{-/-}$ mice (Fig. 5L). These findings suggest that BATF2 affects T cell exhaustion by regulating RGS2 expression.

To further investigate the impact of RGS2 and BATF2 on the growth of lung cancer cells, artificial knockdown of BATF2 or RGS2 was induced in human LC cell lines H1299 and A549. The BATF2 knockdown also resulted in a decrease in RGS2 expression in both cell lines (Fig. S3 A-B). Moreover, in subsequent experiments, we observed that the knockdown of BATF2 or RGS2 in H1299 and A549 cells significantly reduced their proliferation capacity (Fig. S3 C-D). Interestingly, we observed that the knockdown of BATF2 or RGS2 in cancer led to an increase in sensitivity to NK cells, as manifested by increased lactate dehydrogenase (LDH) release (Fig. S3E-F). Additionally, we found that the knockdown of RGS2 or BATF2 significantly reduced the expression of PD-L1, HHLA2, and TIM3 in the two cell lines (Fig. S3G). These results indicate that RGS2 is regulated by BATF2, and the BATF2-RGS2 axis is involved in the growth and immune escape of lung cancer cells.

BATF2 inhibits CXCL13 secretion through transcriptional activation of RGS2

To further elucidate the upstream regulatory mechanism of RGS2, we selected transcription factors specific to each single cell subpopulation (Fig. S4 A), of which MGA, ZNF362, ZNF687, BATF, and ZNF75 A were specifically activated in CD8$^+$ Tex cells (Fig. S4B). The BATF2 transcription factor was the most prominent in CD8$^+$ Tex cells (Fig. S4 C). Similarly, RGS2 was highly expressed in CD8$^+$ Tex cells in the GSE185204 dataset (three anti-PD-1-treated patients with LC) (Fig. S4D-E). A positive correlation between BATF2 and RGS2 expression was observed (Fig. S4 F). After obtaining the RGS2 promoter sequence, we observed the presence of cis-acting elements in the promoter region that interacted with BATF2 (Fig. S4G). The CellChat software package was used to analyze secretory signals after PD-1 blockade therapy in patients with MPR and non-MPR. Patients with MPR had higher CD8$^+$ Tex secretory signals compared to patients with non-MPR, mainly dominated by CXCL and CD137 signals (Fig. S4H-I). CXCL is mainly secreted by CD8$^+$ Tex and acts on CD8$^+$ Tex in a paracrine communication pattern. In the CXCL pathway, the ligand CXCL13 interacts with its receptor CXCR3 (Fig. S4 J-K). CD137 was mainly secreted by precursor exhausted CD8$^+$T cells (Tpex) and acted on CD8$^+$ Tex and CD8$^+$ Tpex, also exhibiting a paracrine communication pattern. In the CD137 pathway, the ligand TNFSF9 interacts with its receptor TNFRSF9 (Fig. S4L-M). Classification based on the topology of the signaling network was used to divide the signaling pathways into four major categories (Fig. S4 N).

Our subsequent experiments showed that the expression levels of CXCL13 were significantly increased in T cells extracted from RGS2$^{-/-}$ and BATF2$^{-/-}$ mice (Fig. 6A-B), a trend that was also confirmed in mouse serum (Fig. 6C). CXCL13 levels in serum may reflect contributions from multiple immune cell types. FACS analysis of tumor-infiltrating immune cells revealed that the population of CD8$^+$ T cells was substantially increased in RGS2$^{-/-}$ and BATF2$^{-/-}$ mice, while the populations of DCs or MDSCs were not significantly changed (Fig. 6D). Previous studies have indicated that CD8$^+$CXCL13$^+$ T cells positively correlated with the efficacy of immune checkpoint blockade (ICB) therapy and a favorable prognosis in tumor patients [17]. Furthermore, the IHC assays demonstrated that the staining intensity of CXCL13 was increased in RGS2$^{-/-}$ mice in both 3LL-formed metastatic nodules in the lung and in the MTO-formed tumors (Fig. 6E-F). To examine whether RGS2 influences T cell exhaustion by inhibiting CXCL13 secretion, the 3LL-innoculated RGS2$^{-/-}$ mice were further administered an anti-mCXCL13 antibody (Am) (Fig. 6G). After Am treatment, the number of tumor nodules formed in the lung tissue of mice was significantly increased (Fig. 6H), along with notable increases in angiogenesis signals (VEGFA and CD31) (Fig. 6I). Moreover, the double-label immunofluorescence assays demonstrated that the population of CD8$^+$GZMB$^+$ T cells was decreased while the population of CD8$^+$VISTA$^+$ cells was increased in the metastatic nodules following Am treatment (Fig. 6J), indicating reduced activation and cytotoxicity of T cells. Similar trends were observed by the FACS (Fig. 6K). Additionally, the staining intensities of PD-1, CTLA4, and Galectin-9 were significantly enhanced after Am treatment as well (Fig. 6L). In vitro, Am treatment of RGS2$^{-/-}$ or BATF2$^{-/-}$ T cells led to a significant reduction in their cytotoxicity against 3LL or KLN205 cells (Fig. 6M-O). These observations suggest that BATF2 promotes RGS2 expression, which in turn inhibits CXCL13 secretion, thereby influencing T cell exhaustion.

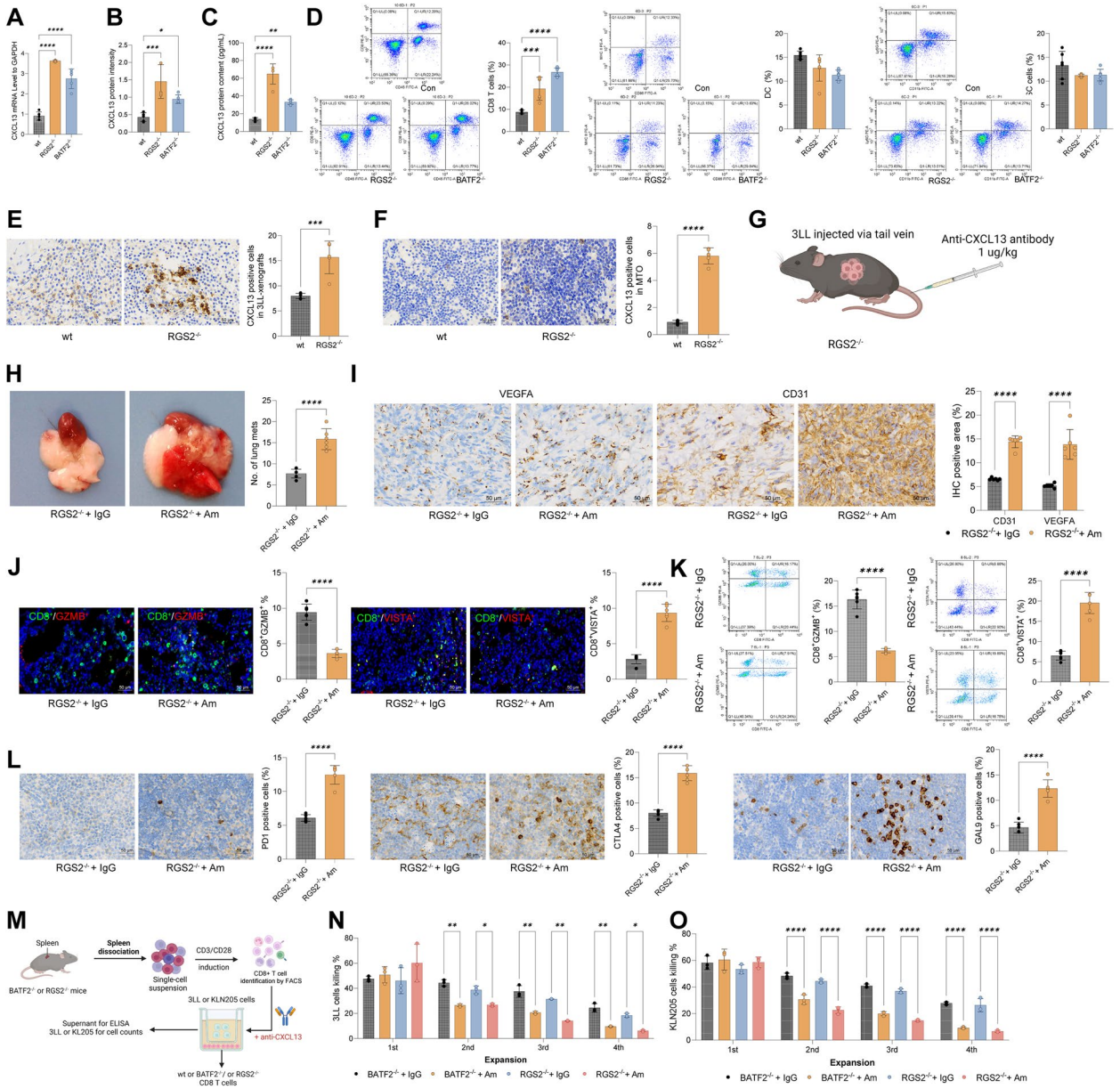

Fig. 6 BATF2 inhibits CXCL13 secretion through transcriptional activation of RGS2. **A-B** mRNA and protein levels of CXCL13 in $CD8^+$ T cells isolated from the spleens of WT, $RGS2^{-/-}$, and $BATF2^{-/-}$ mice. T cells were stimulated with anti-CD3 (2 μg/mL) and anti-CD28 (2 μg/mL) for 48 h before RNA extraction. **C** ELISA to measure the CXCL13 contents in the serum of WT and $RGS2^{-/-}$ or $BATF2^{-/-}$ mice. **D** FACS to measure the populations of $CD8^+$ T cells ($CD3^+CD8^+$), DCs ($CD11c^+CD86^+MHCII^+$), and polymorphonuclear MDSCs ($CD11b^+Ly6G^+$) in the lung tissues. **E–F** IHC to measure the staining intensity for CXCL13 in 3LL-derived metastatic lung nodules or MTO LC tissues. **G** Administration to 3LL-innoculated $RGS2^{-/-}$ mice using an anti-mCXCL13 antibody (Am) or IgG as control. **H** The number of 3LL-formed metastatic nodules in the mice's lung tissues. **I** IHC to measure the staining intensity of VEGFA and CD31 in mouse lung tissues. **J** Immunofluorescence staining to confirm the positive expression and distribution of $CD8^+GZMB^+$ or $CD8^+VISTA^+$ in metastatic nodules in mouse lung tissues. **K** FACS to analyze the proportions of $CD8^+GZMB^+$ or $CD8^+VISTA^+$ T cells in mouse lung tissues. **L** IHC to measure the staining intensity for PD-1, CTLA4, and Galectin-9 in lung tissues. **M** Schematic diagram of the addition of the anti-CXCL13 antibody to the co-culture system of CD3/CD28-stimulated $CD8^+$ T cells from WT, $RGS2^{-/-}$, or $BALF^{-/-}$ mice and mouse 3LL and KLN205 cells. **N–O** the tumor cell killing rates in 1 st-4 th expansion were analyzed. Each dot represents one independent experiment or data from one animal. $^*P < 0.05$, $^{**}P < 0.01$, $^{***}P < 0.001$, $^{****}P < 0.0001$

Higher anti-tumor immune activity in metastasis of BATF2$^{-/-}$ mice

To confirm the effect of BATF2 on the CD8$^+$ T cell activity in LC, we inoculated MTOs into the lung tissues of WT or BATF2$^{-/-}$ mice, followed by treatment of anti-CD8 antibodies (Fig. 7A). Compared to WT mice, the BATF2$^{-/-}$ mice showed substantially reduced number of tumor nodules in their lung tissues as well as reduced tumor metastasis. This reduction was, however, negated by the CD8 clearance (Fig. 7B). IHC showed the positive staining of C-Cas-3, as a marker of apoptosis, was increased in BATF2$^{-/-}$ mice, which was diminished by anti-CD8 treatment as well (Fig 7C). The number of infiltrating CD8$^+$ T cells in the lung tissues was increased upon BATF2 knock-out but reduced following the additional anti-CD8 treatment, whereas the populations of MDSCs or Tregs were not significantly altered (Fig 7D-F). Additionally, BATF2$^{-/-}$ mice exhibited a lower percentage of EpCAM$^+$ cells compared to WT, reflecting reduced tumor epithelial cell presence in the metastatic niche. Following CD8 depletion, EpCAM+ percentages increased in BATF2$^{-/-}$ mice, suggesting that CD8$^+$ T cells play a critical role in controlling the epithelial tumor burden (Fig. 7G). The reduced percentage of EpCAM$^+$ cells in BATF2$^{-/-}$ mice may reflect impaired tumor-immune interactions necessary for epithelial tumor cell survival. CD8 depletion in BATF2$^{-/-}$ mice restores EpCAM+ cell percentages, likely due to the removal of CD8$^+$ T cell-mediated immune pressure on epithelial tumor cells. Furthermore, we observed that the T cell exhaustion markers were reduced whereas the T cell differentiation and function markers were upregulated in both primary and metastatic tumors in BATF2$^{-/-}$ mice, with these effects counteracted by the anti-CD8 treatment again (Fig. 7H-I). Angiogenic signals (CD31 and VEGFA) of primary and metastatic tumors in BATF2$^{-/-}$ mice were also attenuated, but the CD8 clearance restore the angiogenesis (Fig. 7J). Consistently, FACS analysis revealed that BATF2$^{-/-}$ mice had a lower percentage of CD8$^+$ T cells expressing exhaustion markers (PD-1 and TIM3) compared to WT mice, which were further reduced after the anti-CD8 treatment. The number of DCs was not significantly affected upon BATF2 knock-out or CD8 inhibition (Fig. 7K).

Loss of BATF2 blocks T cell exhaustion and increases CD8$^+$ T cell function by suppressing RGS2 expression

We further characterized CD8$^+$ T cell populations in these tumors. Functional CD8$^+$ T cell subsets, specifically GZMB$^+$ cytotoxic CD8$^+$ T cells were significantly enhanced upon BATF2 knock-out, while the VISTA$^+$ Tex were reduced (Fig. 8A-B). The mRNA and protein levels of dysfunctional CD8$^+$ T cell signatures (TIM-3, LAG-3, CD38, 2B4, and TBX21) were notably reduced after BATF2 knock-out. In contrast, the levels of T cell differentiation and function markers (TCF7, CD122, CD127, CD45RA, and CCR7) were elevated (Fig. 8C-D). FACS showed that the proportions of CD68$^+$, IFNγ$^+$, and TCF7$^+$ CD8$^+$ T cells were increased while the proportions of CTLA4$^+$, PDCD1$^+$, and TIM3$^+$ CD8$^+$ T cells were reduced following BTAF2 knock-out. Additionally, single cells were extracted from BTAF2$^{-/-}$ and RGS2$^{-/-}$ mice, followed by anti-CD3/CD28 stimulation (Fig. 8F). Mirroring the findings in tissues, the proportions of IFNγ$^+$ and TCF7$^+$ CD8$^+$ T cells were increased, whereas the populations of CTLA4$^+$, PDCD1$^+$, and TIM3$^+$ CD8$^+$ T were decreased upon BTAF2 or RGS2 knock-out (Fig. 8F-G). FACS files and data are presented in Supplementary file 1.

Discussion

LC is a common malignant tumor that poses a major risk to human life due to its high rates of morbidity and mortality [18]. ICIs are new immunotherapy-based drugs that can improve survival in patients with advanced NSCLC by augmenting the body's natural tumor-killing response [19]. However, T-cell exhaustion has been shown to weaken the efficacy of checkpoint blockade immunotherapies [20]. Consequently, a better understanding of the molecular mechanisms of T-cell exhaustion is of great interest in cancer research. In this study, we found that RGS2 is regulated by BATF2 and contributes to LC progression by potentiating T cell exhaustion and suppressing cytotoxic immune activity (Fig. 9).

(See figure on next page.)

Fig. 7 Higher anti-tumor immune activity in BATF2$^{-/-}$ mice. **A** Schematic representation of MTO inoculation and subsequent treatment with anti-CD8 antibodies in WT and BATF2$^{-/-}$ mice. **B** Gross images of the lung tissues bearing tumor burdens in each group, and number of lymph node metastasis, liver metastasis, and lung metastasis in mice. **C** Positive staining of the apoptosis marker C-Cas-3 in MTO-formed tumor tissues. **D-F** FACS to detect the populations of MDSCs (CD11b$^+$Ly6G$^+$), CD8$^+$ T cells (CD3$^+$CD8$^+$), and Treg (CD3$^+$CD4$^+$CD25$^+$Foxp3$^+$) in MTO-formed tumor tissues. **G** Fluorescence co-localization assay to detect the number of DESMIN$^+$EpCAM$^+$ cells in MTO-formed tumor tissues. **H-I** RT-qPCR and WB to detect the mRNA and protein levels of CD8$^+$ T dysfunction markers (TIM-3, LAG-3, CD38, 2B4, and TBX21) and function markers (TCF7, CD122, CD127, CD45RA, and CCR7). **J** IHC to detect the positive staining of CD31 and VEGFA staining in the MTO-formed tumor tissues. **K** FACS to measure the populations of DCs (CD11c$^+$CD86$^+$MHCII$^+$), CD8$^+$TIM3$^+$ T cells, and CD8$^+$PD-1$^+$ T cells in the MTO-formed tumor tissues. Each dot represents one independent experiment or data from one animal. *$P < 0.05$, **$P < 0.01$, ***$P < 0.001$, ****$P < 0.0001$

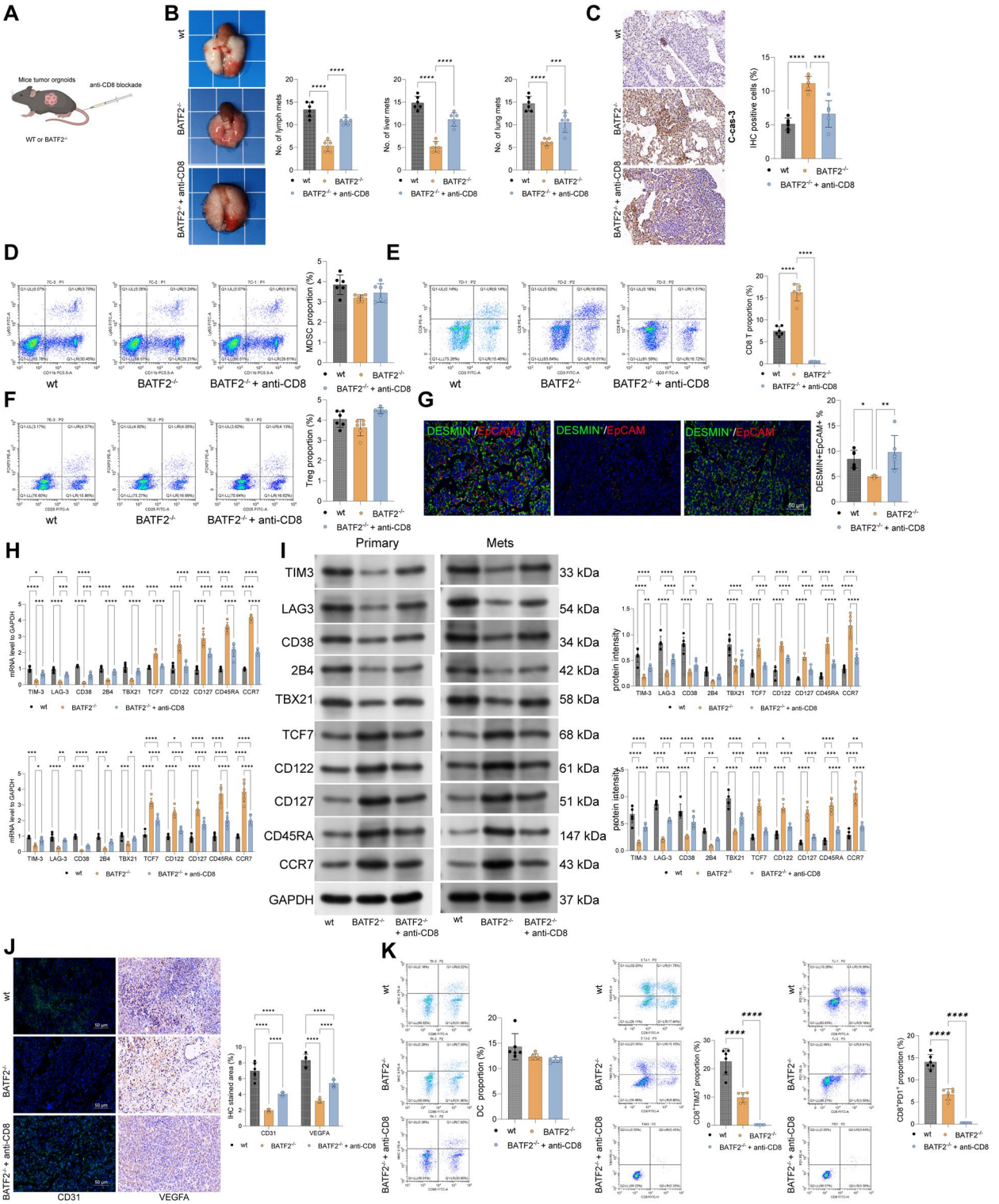

Fig. 7 (See legend on previous page.)

The RGS family of negative regulators of GPCRs have been demonstrated to participate many processes in cancer biology like proliferation, metastasis, and immune activity, making them as potential drug targets for tumor treatment [21, 22]. RGS2 is tightly linked to immune cell infiltration in several cancers, suggesting a global

participation in mediating the tumor immune response in the TME [23]. Nevertheless, studies have highlighted the differential expression patterns of RGS2, either aberrant upregulation [24, 25] or downregulation [26, 27], in human malignancies, suggesting its context-dependent role in cancer progression. In bladder cancer, RGS2 has been suggested as a pyroptosis-related gene linking to cancer progression, poor diagnosis, and immunological alteration [28]. In NSCLC. high expression of RGS2 has been linked to poor prognosis as well, and targeting RGS2 after chemotherapy has been suggested to reduce cancer recurrence [11]. However, the roles of RGS2 in immune activity in LC remains largely unknown.

In this study, our integrated bioinformatics analyses identified increased RGS2 expression in $CD8^+$ Tex cells, which primarily mediated hematopoiesis and leukocyte differentiation and was predominantly enriched in the NF-κB pathway. GSEA analysis suggested that high RGS2 expression activated several pathways such as TNFA signaling via NFKB, allograft rejection, and inflammatory response, all of which are important immune response-related pathways in cancers [29, 30]. Activation of the NF-κB pathway facilitates $CD8^+$ T-cell exhaustion in diverse tumors [31–35]. A recent study by Joshi and colleagues demonstrated that RGS2 functions as an innate immune checkpoint that reduces Gαq-mediated IFNγ production in lung injury [36]. A pan-cancer analysis by Yang *et al.* suggested a significant association between RGS2 expression and tumor mutation burden, TIDE, and $CD8^+$ T infiltration in many cancer types [23]. This evidence suggests a possible correlation between RGS2 and immunosuppression in LC.

Our first functional experiments showed that the knock-out of RGS2 in mice led to a significant reduction in lung and liver metastasis in the setting of tail vein injection of 3LL cells. Additionally, in a primary LC model induced by MCA, increased RGS2 staining was detected in tumor tissues compared to non-cancerous lung tissues, and greater RGS2 staining was determined in metastatic tissues. This evidence suggests the possible correlations between RGS2 expression and the initiation and metastasis of lung tumors. RGS proteins in lymphocytes are critical regulators of lymphocyte migration, function, and chemokine receptor signaling [37]. Earlier studies have demonstrated that RGS2 plays a critical role in T cell activation and synapse development in the hippocampus [38]. In cancer immunity, T cell exhaustion is primarily characterized by poor proliferative potential, low effector cytokine secretion, and expression of inhibitory receptors on the cell surface (such as PD-1, LAG3, CTLA4, and TIM3), which reduce the effectiveness of T cell-mediated immunity [20, 39–42]. Notably, we observed that the $RGS2^{-/-}$ mice showed significantly reduced populations of $PD\text{-}1^+$, $CTLA4^+$, and $TIM3^+CD8^+$ T cells, supporting the concept that RGS2 is primarily correlated with Tex cells in LC. Similar trends were observed in another MTO model in $RGS2^{-/-}$ mice. Consistently, $CD8^+$ T cells isolated from $RGS2^{-/-}$ exhibited lower expression of these exhaustion markers *in vitro* while showing increased immune active cytokines (IL-2, GZMB, TNFA, and IFNγ) in the culture system. Elevated levels of RGS2 result in immune rejection and dysfunction in gastric cancer [23]. Boelte and team members also suggested the RGS2 knock-out contributes to a significant delay in tumor progression in mice [43]. They also ascribed the immunosuppressive role of RGS2 to the maintenance of pro-angiogenic function of MDSCs [43]. However, we observed that the populations of other types of immunoregulatory cells, like DCs or MDSCs, were not significantly altered in $RGS2^{-/-}$ mice, indicating that the RGS2 axis primarily affects $CD8^+$ T cells to modulate immune activity in the TME of LC. Nevertheless, it should be clarified that while the numbers of DCs or MDSCs were not significantly changed, their activity or function could be affected upon RGS2 loss, which awaits further investigation.

RGS2 has been recognized as a negative mediator of STAT3-mediated Nox1 expression, while Nox1 expression can facilitate TLR-mediated activation of innate immunity [44]. This might be one of the mechanisms of RGS2-mediated immunosuppression. Importantly, we observed that $RGS2^{-/-}$ mice had reduced phosphorylation of p65, JNK and p38, which are key immunosuppressive modulators by upregulating PD-L1 expression [45, 46]. The bioinformatics analyses concerning the mechanisms underlying RGS2's function revealed BATF2 as

(See figure on next page.)

Fig. 8 Loss of BATF2 blocks T cell exhaustion and increases $CD8^+$ T cell function in primary and metastatic tissues. **A-B** Immunofluorescence staining to confirm the positive expression and distribution of $CD8^+GZMB^+$ or $CD8^+VISTA^+$ in mouse primary lung tumors and liver metastatic tumors. **C-D** RT-qPCR and WB to detect the mRNA and protein levels of $CD8^+$ T dysfunction markers (TIM-3, LAG-3, CD38, 2B4, and TBX21) and function markers (TCF7, CD122, CD127, CD45RA, and CCR7). **E** FACS to identify the populations of $CD8^+CD69^+$, $CD8^+IFN\gamma^+$, $CD8^+TCF7^+$, $CD8^+CTLA4^+$, $CD8^+PD1^+$, and $CD8^+TIM3^+$ cells in the primary lung tumors and liver metastatic tumors. **F** Schematic diagram of the isolation of spleen lymphocytes from WT, $BATF2^{-/-}$, and $RGS2^{-/-}$ mice and stimulation of CD3/CD28 antibodies to induce T cells. **G-H** FACS to identify the populations of $CD8^+CD69^+$, $CD8^+IFN\gamma^+$, $CD8^+TCF7^+$, $CD8^+CTLA4^+$, $CD8^+PD1^+$, and $CD8^+TIM3^+$ subsets in the extracted cells. Each dot represents one independent experiment or data from one animal. $^*P < 0.05$, $^{**}P < 0.01$, $^{***}P < 0.001$, $^{****}P < 0.0001$

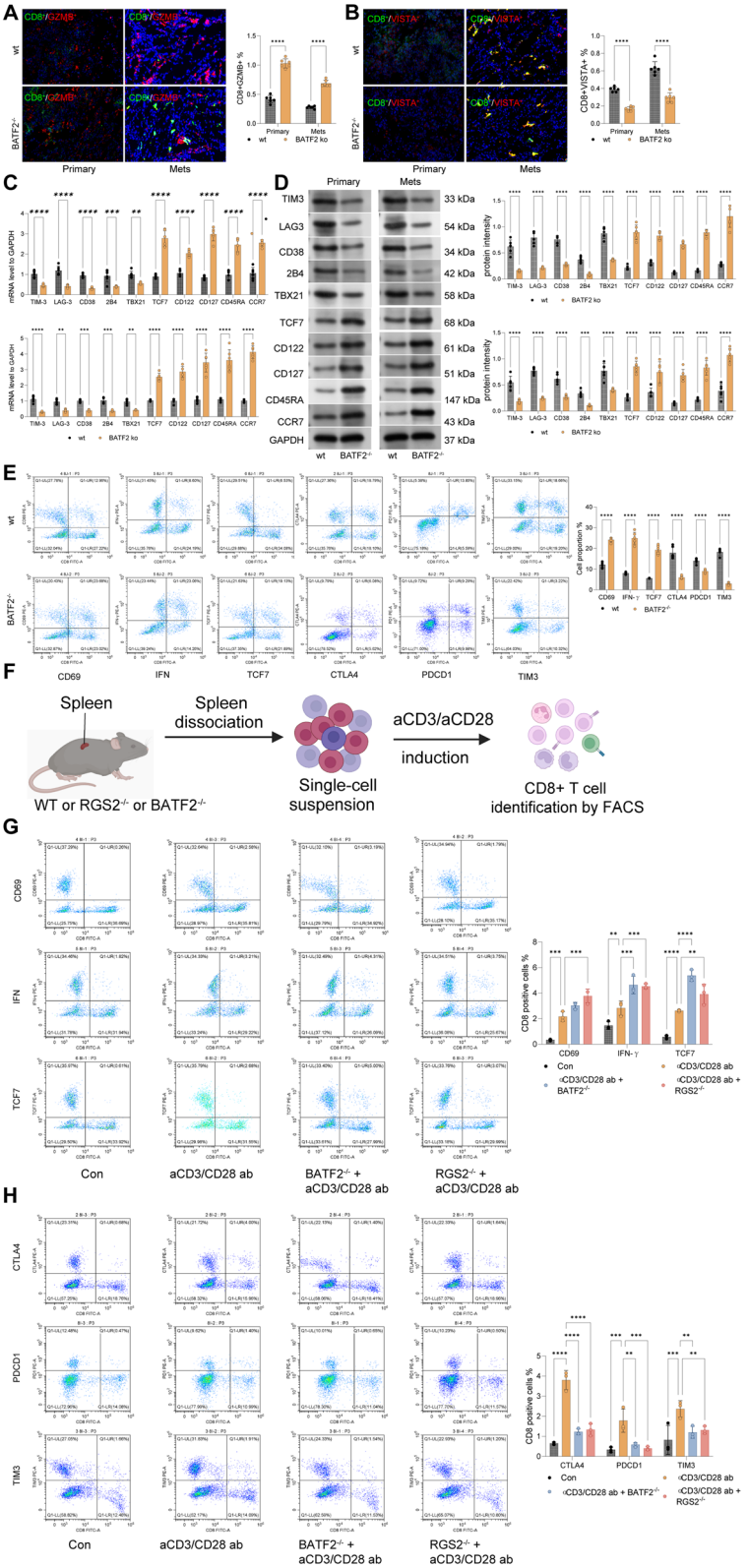

Fig. 8 (See legend on previous page.)

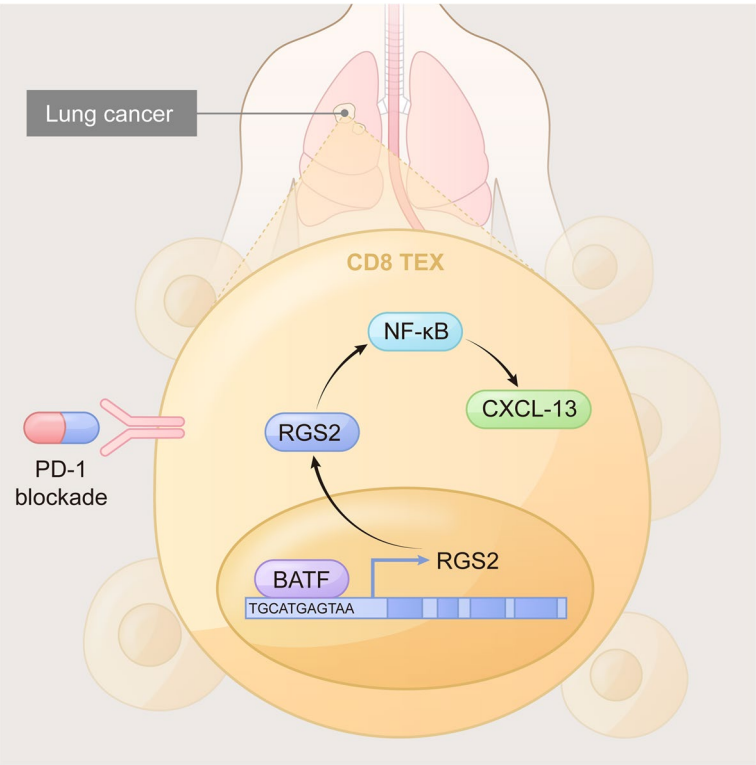

Fig. 9 Graphical abstract. A schema showing BATF2 binds to the RGS2 promoter and activates its transcription. Knockout of BATF2 or RGS2 reduces exhaustion and improves anti-tumor immunity of $CD8^+$ T cells in LC through CXCL13 activation

its important upstream regulator and CXCL13 a downstream signaling suppressed by the BATF2/RGS2 axis. Indeed, the luciferase assays confirmed the role of BATF2 in activating RGS2 transcription, and BATF2 overexpression plasmids led to increased RGS2 mRNA and protein levels in cells in a concentration-dependent manner.

Interestingly, both BATF and RGS2 have been suggested as $CD8^+$ T cell-associated signature genes in hepatocellular carcinoma, linking to immune dysregulation and poor prognosis in patients [47]. In fact, BATF2 has been suggested to exert diverse and context-dependent immunoregulatory functions in health and disease [48]. Interestingly, in HIV-specific $CD8^+$ T cells, BATF upregulation has been responsible for PD-1-mediated T cel exhaustion [49]. While Liu *et al.* identified that BATF2 reduced PD-L1 expression in NSCLC cells, predisposing cancer cells to immune cell cytotoxicity [50]. We observed that that T cells extracted from $BATF2^{-/-}$ mice showed enhanced cytotoxicity on KLN205 and 3LL cells after the 2^{nd} expansion. Additionally, $BATF2^{-/-}$ mice presented similar phenotypes as $RGS2^{-/-}$ mice, including increased CD8+ T cell population, reduced tumor growth and metastasis in animal models, and reduced expression of T cell exhaustion markers while increased expression of T cell function markers in the MTO-derived tumors. Partly consistent with this, depletion of BATF has been found to enhance anti-tumor effects and reduce exhaustion of CAR-T cells [14, 51]. Notably, the CXCL13 signaling was activated upon either BATF2 or RGS2 knockout. CXCL13 is a chemokine that plays a key role in immune cell trafficking and activation. By binding to its receptor CXCR5 expressed on $CD8^+$ T cells, CXCL13 facilitates the migration of these T cells from peripheral blood into the TME, where they can engage and attack tumor cells [17, 52]. The facts that an inhibitory antibody of CXCL13 restored tumor metastasis and increased Tex populations in $RGS2^{-/-}$ mice suggests that CXCL13 is fundamental for immune activity in the TME of LC upon BATF2 or RGS2 loss.

It was noted that the numbers of MDSCs or DCs were not significantly altered in mice with $BATF2^{-/-}$. Also, we observed that $BATF2^{-/-}$ or $RGS2^{-/-}$ mice showed a reduced population of $CD8^+$ T cells in their lung tissues and that T cells extracted from these mice showed increased cytotoxicity to LC cell lines in co-culture systems. Additional treatment of anti-CD8 negated this reduction, verifying that BATF2/RGS2 primarily affect immune activity by influence T cells. Nevertheless, RGS2 has been identified as a potential biomarker expressed in gastric cancer cells and linked to an immunosuppressive condition

[23]. Notably, we observed that the direct knockdown of RGS2 or BATF2 in LC cells suppressed tumor malignant phenotype and reduced resistance to NK cell cytotoxicity. This evidence suggests that the BATF2/RGS2 axis can drive malignant properties of tumor cells directly and, in the meantime, they reduce the abundance and activity of $CD8^+$ T cells to drive immunosuppression.

However, additional experiments are required to confirm that T cells are the primary driver of the tumor rejection phenotype. For instance, depleting $CD8^+$ T cells in $RGS2^{-/-}$ mice should reverse the tumor rejection phenotype to WT levels. Alternatively, adoptive transfer of WT or $RGS2^{-/-}$T cells into tumor-bearing WT mice will allow us to directly assess the contribution of RGS2-deficient T cells to tumor immunity. Unfortunately, the financial and time constraints prevented us from performing additional animal experiments at the present stage. Additionally, while we identified $CD8^+$ cells from spleen lymphocytes after CD3/CD28 stimulation, this $CD8^+$ T cell subset was not sorted or purified for subsequent experiments. Although the current experimental setup allowed us to analyze the proportion and trends of specific $CD8^+$ T cell populations, using purified 100% $CD8^+$ T cells would be a more optimized approach. We will address these limitations in future investigation endeavors to provide deeper insights into the oncogenic roles of the BATF2/RSF2 cascade in LC.

In conclusion, this study demonstrates that BATF2 elevated RGS2 expression to accelerate T cell exhaustion and to repress anti-tumour immune activity by inhibiting the CXCL13 signaling. Combining this strategy with ICIs or anti-angiogenic agents could offer synergistic benefits, improving outcomes in patients with immune-resistant tumors.

Abbreviations

RGS2	Regulator of G Protein Signaling 2
BATF2	Basic Leucine Zipper ATF-like Transcription Factor
NF-κB	Nuclear Factor kappa-light-chain-enhancer of activated B cells
TME	Tumor Microenvironment
LC	Lung Cancer
$CD8^+$Tex	$CD8^+$T cells, exhausted
ICIs	Immune Checkpoint Inhibitors
PD-1	Programmed Death-1
PD-L1	Programmed Death-Ligand 1
CTLA4	Cytotoxic T-Lymphocyte-Associated Protein 4
TME	Tumor Microenvironment
PCA	Principal Component Analysis
UMAP	Uniform Manifold Approximation and Projection
t-SNE	T-Distributed Stochastic Neighbor Embedding
GSEA	Gene Set Enrichment Analysis
MPR	Major Pathologic Response
DEGs	Differentially Expressed Genes
RT-qPCR	Real Time-Quantitative Polymerase Chain Reaction
WB	Western Blotting
CFU	Colony Forming Unit
EdU	5-Ethynyl-2′-deoxyuridine
shRNA	Short Hairpin RNA
MCA	Methylcholanthrene
DSA	Digital Subtraction Angiography
DMEM	Dulbecco's Modified Eagle Medium
MTO	Murine Tumor Organoid
OBM	Organoid Basic Medium
RIPA	Radioimmunoprecipitation Assay
BCA	Bicinchoninic Acid
PVDF	Polyvinylidene Fluoride
ECL	Enhanced Chemiluminescence
NK	Natural Killer
IFN-γ	Interferon Gamma
FACS	Fluorescence-Activated Cell Sorting
IHC	Immunohistochemistry
ANOVA	Analysis of Variance
TIDE	Tumor Immune Dysfunction and Exclusion
KO	Knock-out
TCR	T Cell Receptor
TIM-3	T-cell immunoglobulin and mucin-domain containing-3
LAG-3	Lymphocyte Activation Gene-3
MDSCs	Myeloid-Derived Suppressor Cells
STAT3	Signal Transducer and Activator of Transcription 3
TLR	Toll-like Receptor
MCP-1	Monocyte Chemoattractant Protein-1
CAR-T	Chimeric Antigen Receptor T-cell
EpCAM	Epithelial Cell Adhesion Molecule
VEGFA	Vascular Endothelial Growth Factor A
TNF-a	Tumor Necrosis Factor Alpha
CD69	Cluster of Differentiation 69
CXCL13	Chemokine (C-X-C Motif) Ligand 13
CCR7	C-C Chemokine Receptor Type 7

Supplementary Information

The online version contains supplementary material available at https://doi.org/10.1186/s12943-025-02351-5.

Supplementary Material 1: Fig. S1. RGS2 knockout promotes CD8 T cells function. A, immunofluorescence staining to analyze the positive staining of RGS2 and CD8 in the lung tissues of WT or RGS2-/- mice upon tail vein injection of mouse 3LL cells; B-C, ELISA to measure the contents of cytokines (IL-2, IFN-γ, GZMB, and TNFA) released by T cells. Each dot represents data from one animal. ***$P < 0.001$, ****$P < 0.0001$.

Supplementary Material 2: Fig. S2. RGS2 is linked to growth, metastasis, and poor patient outcome in LC. A-B, Positive staining area of RGS2 in the normal tissue, primary tumor tissue, and metastatic tumor tissues in the mouse model of MCA-induced primary LC. C, Positive staining of RGS2 in normal tissue, and primary and metastatic tumor tissues in mice determined using immunofluorescence staining. D, RGS2 mRNA expression in normal tissue, and primary and metastatic tumor tissues in mice determined using RT-qPCR. E-F, Correlation between RGS2 level and liver or lymph node metastasis in LC patients according to TCGA database. G, Correlation between RGS2 and survival of LC patients in TCGA database. Each dot represents data from one animal. ***$P < 0.001$, ****$P < 0.0001$.

Supplementary Material 3: Fig. S3. Knockdown of BATF2 or RGS2 suppressed LC growth in vitro. A, Knockdown of RGS2 or BATF2 was induced in H1299 and A549 cells. B, A plate clone formation assay was conducted to evaluate the clonogenic ability of H1299 and A549 cells. C, EdU assay to evaluate the DNA replication ability of H1299 and A549 cells. D~E, Co-culture of H1299 or A549 cells with NK92 cells, followed by LDH assay to assess tumor cell lysis. F, qPCR to detect the expression levels of the immune escape markers PD-L1, HHLA2, and TIM3 in H1299 and A549 cells. Three cycles of the tests were conducted, and the results are presented as mean ± SD. One-way or two-way ANOVA was used for statistical analysis, and Tukey's multiple comparison test was used for post hoc analysis. ******$P < 0.0001$, **$P < 0.01$, ***$P < 0.001$.

Supplementary Material 4: Fig S4. Transcription factor and cell communication analysis in CD8+ T cells. A, Heatmap of transcription factor expression specific to individual subgroups of CD8+ T cells. B, Transcription factors MGA, ZNF362, ZNF687, BATF, and ZNF75A are specifically activated in CD8+ Tex cells. C, Expression of MGA, ZNF362, ZNF687, BATF, and

ZNF75A in various subgroups, with BATF being significantly expressed in CD8+ Tex cells. D–E, Validation of RGS2 gene expression in the GSE185204 dataset, showing high expression of RGS2 in CD8+ Tex cells. F, Correlation of BATF2 transcription factor expression with RGS2 expression. G, Presence of cis-regulatory elements in the RGS2 promoter region that interact with BATF. H, Analysis of signal secretion differences between PD-1 blockade treatment responders (MPR) and non-responders (non-MPR). I, Higher signal secretion in patients with MPR of CD8+ Tex compared to that in patients with non-MPR, primarily involving CXCL and CD137 signaling. J, Communication patterns of the CXCL signalling pathway in CD8+ T cell subgroups. K, Roles of CXCL signaling in CD8+ T cell subgroups and the contribution of each ligand-receptor pair to the overall signaling pathway. L, Communication patterns of the CD137 signaling pathway in the CD8+ T cell subgroups. M, Roles of CD137 signaling in CD8+ T cell subgroups and the contribution of each ligand-receptor pair to the overall signaling pathway. N, Classification of the topological structure of the signaling network.

Authors' contributions

X.G. contributed significantly to the overall structure and content of the manuscript and C.G. and X.S. were responsible for conducting the experimental work and Y.Z. played a crucial role in the data analysis and interpretation and Q.F. and J.Y. assisted in the preparation of the manuscript and Z.W. performed validation and formal analysis, and assisted in the investigation and D.Z. and W.Z. served as the principal investigators of the study, overseeing the research and providing guidance throughout the entire process. All authors reviewed the manuscript. All authors reviewed the manuscript.

Funding

This study was supported by the Youth Found of the National Natural Science Foundation of China (82103309).
Youth Found of the National Natural Science Foundation of China,82103309

Data availability

No datasets were generated or analysed during the current study.

Declarations

Ethics approval and consent to participate

This study and included experimental procedures were approved by the institutional animal care and use committee of Zhongda Hospital, School of Medicine, Southeast University (approval NO.20210301085). All animal housing and experiments were conducted in strict accordance with the institutional guidelines for the care and use of laboratory animals.

Competing interests

The authors declare no competing interests.

Received: 22 October 2024 Accepted: 9 May 2025
Published online: 30 May 2025

References

1. Thai AA, et al. Lung cancer. Lancet. 2021;398(10299):535–54.
2. Schabath MB, Cote ML. Cancer progress and priorities: lung cancer. Cancer Epidemiol Biomarkers Prev. 2019;28(10):1563–79.
3. Bade BC, Dela Cruz CS. Lung cancer 2020: epidemiology, etiology, and prevention. Clin Chest Med. 2020;41(1):1–24.
4. Wadowska K, et al. Genetic markers in lung cancer diagnosis: a review. Int J Mol Sci. 2020;21(13):4569.
5. Lahiri A, et al. Lung cancer immunotherapy: progress, pitfalls, and promises. Mol Cancer. 2023;22(1):40.
6. Shiravand Y, et al. Immune Checkpoint Inhibitors in Cancer Therapy. Curr Oncol. 2022;29(5):3044–60.
7. Ai L, Xu A, Xu J. Roles of PD-1/PD-L1 pathway: signaling, cancer, and beyond. Adv Exp Med Biol. 2020;1248:33–59.
8. Chow A, et al. Clinical implications of T cell exhaustion for cancer immunotherapy. Nat Rev Clin Oncol. 2022;19(12):775–90.
9. Zhang Q, Haak AJ, Sjogren B. Regulator of G protein signaling 2 inhibits Galpha(q)-dependent uveal melanoma cell growth. J Biol Chem. 2022;298(6): 101955.
10. McNabb HJ, Zhang Q, Sjögren B. Emerging roles for regulator of G protein signaling 2 in (Patho)physiology. Mol Pharmacol. 2020;98(6):751–60.
11. Cho J, et al. RGS2-mediated translational control mediates cancer cell dormancy and tumor relapse. J Clin Invest. 2021;131(1):e171901.
12. Wang D. The essential role of G protein-coupled receptor (GPCR) signaling in regulating T cell immunity. Immunopharmacol Immunotoxicol. 2018;40(3):187–92.
13. Man K, et al. Transcription factor IRF4 promotes CD8(+) T cell exhaustion and limits the development of memory-like T cells during chronic infection. Immunity. 2017;47(6):1129-1141.e5.
14. Zhang, X., et al., Depletion of BATF in CAR-T cells enhances antitumor activity by inducing resistance against exhaustion and formation of central memory cells. Cancer Cell, 2022. 40(11): p. 1407–1422 e7.
15. Yoshihara K, et al. Inferring tumour purity and stromal and immune cell admixture from expression data. Nat Commun. 2013;4:2612.
16. Jiang P, et al. Signatures of T cell dysfunction and exclusion predict cancer immunotherapy response. Nat Med. 2018;24(10):1550–8.
17. Liu B, et al. Single-cell meta-analyses reveal responses of tumor-reactive CXCL13(+) T cells to immune-checkpoint blockade. Nat Cancer. 2022;3(9):1123–36.
18. Xie S, et al. The metastasizing mechanisms of lung cancer: recent advances and therapeutic challenges. Biomed Pharmacother. 2021;138: 111450.
19. Suresh K, et al. Immune checkpoint immunotherapy for non-small cell lung cancer: benefits and pulmonary toxicities. Chest. 2018;154(6):1416–23.
20. Belk JA, Daniel B, Satpathy AT. Epigenetic regulation of T cell exhaustion. Nat Immunol. 2022;23(6):848–60.
21. Hu Y, et al. Identification of a five-gene signature of the RGS gene family with prognostic value in ovarian cancer. Genomics. 2021;113(4):2134–44.
22. Hurst JH, Hooks SB. Regulator of G-protein signaling (RGS) proteins in cancer biology. Biochem Pharmacol. 2009;78(10):1289–97.
23. Yang S, et al. Fatty acid metabolism is related to the immune microenvironment changes of gastric cancer and RGS2 is a new tumor biomarker. Front Immunol. 2022;13: 1065927.
24. Smalley MJ, et al. Regulator of G-protein signalling 2 mRNA is differentially expressed in mammary epithelial subpopulations and over-expressed in the majority of breast cancers. Breast Cancer Res. 2007;9(6):R85.
25. Zhu Y, et al. Investigatory and analytical approaches to differential gene expression profiling in mantle cell lymphoma. Br J Haematol. 2002;119(4):905–15.
26. Hurst JH, Mendpara N, Hooks SB. Regulator of G-protein signalling expression and function in ovarian cancer cell lines. Cell Mol Biol Lett. 2009;14(1):153–74.
27. Cao X, et al. Regulator of G-protein signaling 2 (RGS2) inhibits androgen-independent activation of androgen receptor in prostate cancer cells. Oncogene. 2006;25(26):3719–34.
28. Xu J, et al. Constructing and validating a pyroptosis-related genes prognostic signature for stomach adenocarcinoma and immune infiltration: potential biomarkers for predicting the overall survival. J Oncol. 2022;2022:3102743.
29. Huang YC, et al. High expression of interferon pathway genes CXCL10 and STAT2 is associated with activated T-Cell signature and better outcome of oral cancer patients. J Pers Med. 2022;12(2):140.
30. Alumkal JJ, et al. Transcriptional profiling identifies an androgen receptor activity-low, stemness program associated with enzalutamide resistance. Proc Natl Acad Sci U S A. 2020;117(22):12315–23.
31. Rong D, et al. MGP promotes CD8(+) T cell exhaustion by activating the NF-κB pathway leading to liver metastasis of colorectal cancer. Int J Biol Sci. 2022;18(6):2345–61.
32. Sasidharan Nair V, et al. Transcriptomic profiling of tumor-infiltrating CD4(+)TIM-3(+) T cells reveals their suppressive, exhausted, and metastatic characteristics in colorectal cancer patients. Vaccines (Basel). 2020;8(1):71.

33. Zhang Z, et al. PER2 binding to HSP90 enhances immune response against oral squamous cell carcinoma by inhibiting IKK/NF-κB pathway and PD-L1 expression. J Immunother Cancer. 2023;11(11):e007627.
34. Larrayoz M, et al. Preclinical models for prediction of immunotherapy outcomes and immune evasion mechanisms in genetically heterogeneous multiple myeloma. Nat Med. 2023;29(3):632–45.
35. Liu X, et al. CRIP1 fosters MDSC trafficking and resets tumour microenvironment via facilitating NF-κB/p65 nuclear translocation in pancreatic ductal adenocarcinoma. Gut. 2023;72(12):2329–43.
36. Joshi JC, et al. RGS2 is an innate immune checkpoint for suppressing Galphaq-mediated IFNgamma generation and lung injury. iScience. 2025;28(2):111878.
37. Moratz C, Harrison K, Kehrl JH. Regulation of chemokine-induced lymphocyte migration by RGS proteins. Methods Enzymol. 2004;389:15–32.
38. Oliveira-Dos-Santos AJ, et al. Regulation of T cell activation, anxiety, and male aggression by RGS2. Proc Natl Acad Sci U S A. 2000;97(22):12272–7.
39. Dixon KO, Lahore GF, Kuchroo VK. Beyond T cell exhaustion: TIM-3 regulation of myeloid cells. Sci Immunol. 2024;9(93):eadf2223.
40. Sun C, Li D, Wang Z. BATF-mediated regulation of exhausted CD8(+) T-cell responses and potential implications for chimeric antigen receptor-T therapy. Immunotherapy. 2024;16(5):331–40.
41. Hashimoto M, Ramalingam SS, Ahmed R. Harnessing CD8 T cell responses using PD-1-IL-2 combination therapy. Trends Cancer. 2024;10(4):332–46.
42. Pan X, et al. Metabolic plasticity of T cell fate decision. Chin Med J (Engl). 2024;137(7):762–75.
43. Boelte KC, et al. Rgs2 mediates pro-angiogenic function of myeloid derived suppressor cells in the tumor microenvironment via upregulation of MCP-1. PLoS ONE. 2011;6(4): e18534.
44. Lee HK, et al. RGS2 is a negative regulator of STAT3-mediated Nox1 expression. Cell Signal. 2012;24(3):803–9.
45. Jin X, et al. Phosphorylated RB promotes cancer immunity by inhibiting NF-kappaB activation and PD-L1 expression. Mol Cell. 2019;73(1):22-35 e6.
46. Ni Z, et al. JNK signaling promotes bladder cancer immune escape by regulating METTL3-mediated m6A modification of PD-L1 mRNA. Cancer Res. 2022;82(9):1789–802.
47. Li X, et al. Development of a novel CD8(+) T cell-associated signature for prognostic assessment in hepatocellular carcinoma. Cancer Control. 2024;31:10732748241270584.
48. van der Geest R, Lee JS. Role of the basic leucine zipper transcription factor BATF2 in modulating immune responses and inflammation in health and disease. J Leukoc Biol. 2025;117(3):qiae245.
49. Quigley M, et al. Transcriptional analysis of HIV-specific CD8+ T cells shows that PD-1 inhibits T cell function by upregulating BATF. Nat Med. 2010;16(10):1147–51.
50. Liu J, et al. BATF2 inhibits PD-L1 expression and regulates CD8+ T-cell infiltration in non-small cell lung cancer. J Biol Chem. 2023;299(11): 105302.
51. Jiang P, et al. Single-cell ATAC-seq maps the comprehensive and dynamic chromatin accessibility landscape of CAR-T cell dysfunction. Leukemia. 2022;36(11):2656–68.
52. Yang M, et al. CXCL13 shapes immunoactive tumor microenvironment and enhances the efficacy of PD-1 checkpoint blockade in high-grade serous ovarian cancer. J Immunother Cancer. 2021;9(1):e001136.

Publisher's Note